Cement and Concrete Composites 150 (2024) 105545

Contents lists available at ScienceDirect

Cement and Concrete Composites

journal homepage: www.elsevier.com/locate/cemconcomp

Effect of steel fibre with different orientations on mechanical properties of 3D-printed steel-fibre reinforced concrete: Mesoscale finite element analysis

Yekai Yang [a], Pengyuan Lu [a], Zhongxian Liu [c,**], Liang Dong [c], Jianjun Lin [a], Ting Yang [d], Quanchang Ren [c], Chengqing Wu [b,*]

[a] *State Key Laboratory of Metastable Materials Science and Technology, Yanshan University, Qinhuangdao, 066000, China*
[b] *School of Civil and Environmental Engineering, University of Technology Sydney, Sydney, NSW, 2007, Australia*
[c] *Tianjin Key Laboratory of Civil Structure Protection and Reinforcement, Tianjin Chengjian University, Tianjin, 300384, China*
[d] *Protective Structures Centre, Guangzhou University, Guangzhou, 510006, China*

ARTICLE INFO

Keywords:
3D printing
SFRC
Fibre orientation
Mesoscale finite element analysis
Anisotropic

ABSTRACT

It is widely recognized that steel fibres exhibit directional distribution during the preparation of 3D-printed steel fibre reinforced concrete (SFRC). The degree of fibre orientation varies due to several factors, such as nozzle size and layer height. This variation in fibre orientation range may result in different mechanical performance exhibited by 3D-printed SFRC at hardened state. To explore the relationship between steel fibre orientation and the mechanical properties of 3D-printed SFRC at hardened state, this study firstly establishes three-dimensional mesoscale finite element models based on the distribution of fibres in 3D-printed SFRC. The steel fibre and matrix work together through a mechanism for fluid-structure interaction between models. Then, compares the simulation results with experimental data to verify the accuracy of the models. After that, different steel fibre distribution orientations were set, and parametric analysis was conducted for the compressive and tensile loading conditions to explore the effects of fibre orientation on the damage mode and strength of 3D-printed SFRC. The results indicate that 3D-printed SFRC exhibits different damage modes with varying steel fibre orientation ranges. Additionally, the strength of 3D-printed SFRC varies in steel fibre orientation range and exhibits anisotropic characteristics. This study provides a theoretical basis for improving and controlling the performance of 3D-printed SFRC in future engineering applications.

The main acronym parameters used in the paper are summarized in the following table：

Acronym parameters	Meaning
θ	Angles between the projection of steel fibre on XOY plane and X-axis
η	Angles between the projection of steel fibre on XOZ plane and X-axis
V_{sp}	The generated steel fibre space volume
C_{sf}	The steel fibre volume content
L_{sf}	The steel fibre length
D_{sf}	The steel fibre diameter
N_{sf}	The target number of steel fibres
$\Delta\sigma_y$	Maximum yield surface
$\Delta\sigma_m$	Maximum strength surface
$\Delta\sigma_r$	Residual strength surface
p	Hydrostatic pressure
a-parameters	Parameters for determining the strength surfaces
λ	Modified effective plastic strain
$\varphi(\lambda)$	Interpolation function of λ
σ_y	Yield strength
σ_0	Initial yield strength
E_p	Plastic hardening modulus
ε_{eff}^{p}	Effective plastic strain
β	A hardening parameter

(*continued on next column*)

(*continued*)

(*continued on next page*)

---

* Corresponding author.
** Corresponding author.
E-mail addresses: zhongxian1212@163.com (Z. Liu), Chengqing.wu@uts.edu.au (C. Wu).

https://doi.org/10.1016/j.cemconcomp.2024.105545
Received 3 February 2024; Received in revised form 28 March 2024; Accepted 11 April 2024

(*continued*)

Acronym parameters	Meaning
E	Elastic modulus
E_t	Tangent modulus
G_s	Bond shear modulus
D	Damage parameter

1. Introduction

In recent years, there has been increasing interest in the advancement of 3D-printed concrete technology in the field of construction engineering. This technology offers numerous advantages, such as minimizing formwork loss, optimizing labour allocation, and reducing carbon emissions [1–3]. The development of 3D-printed concrete technology relies heavily on the selection of suitable concrete materials. Specifically, the materials used for 3D printing should possess desirable fresh properties and exhibit favourable mechanical properties upon hardening. Extensive research has been conducted by scholars to investigate the material characteristics of 3D-printed concrete (3DPC) [4–8]. Further exploration has revealed that 3DPC tends to consume a larger amount of cement as compared to traditional concrete, which in turn, may result in drying shrinkage concerns [9–11]. Additionally, automated arrangement of steel bars in 3D-printed concrete without human intervention remains challenging, thereby limiting its ductility potential.

To solve these problems, scholars generally use adding fibres in slurry to improve the performance of 3DPC [12–14]. Among them, 3D-printed steel fibre-reinforced concrete (SFRC) is the most widely studied [15–18]. For example, Pham et al. [19] investigated the effect of steel fibres with different lengths (3 mm and 6 mm) on the mechanical properties of high-performance printing concrete with different fibre volume fractions (0.25 %, 0.5 %, 0.75 %, and 1 %). The experimental results reveal that the critical length and volume fraction of fibres, especially 0.75 % and 1 % of 6 mm long steel fibres, as well as the orientation of fibres, are important factors for improving the flexural resistance. Singh et al. [20] studied the compressive properties of steel fibre filled 3D-printed concrete under different loading directions. The authors believed that the mixture with 0.75 % steel fibre has the highest compressive strength when the loading direction is perpendicular to the printing direction. Giwa et al. [21] explored the hardening properties of 3D-printed cementitious materials with different steel fibre content, especially high steel fibre content. Their research demonstrates that when the fibre content is high, the mechanical properties of the reinforced mixture are significantly improved. Chen et al. [22] studied the distribution of steel fibre in 3D-printed coarse aggregate concrete. They found that the mechanical anisotropy of 3D-printed SFRC became less pronounced due to the change in the directional distribution of steel fibres caused by coarse aggregates. At present, extensive studies have elucidated the presence of anisotropic effects, particularly with regards to tensile strength, in 3D-printed fibre-reinforced concrete. Scholars widely attribute this phenomenon to the directional distribution of steel fibres within the 3D-printed concrete [12,23]. In our previous research, a series of investigations were conducted on 3D-printed ultra-high performance steel fibre-reinforced concrete [15–17]. The findings from our studies also confirm the influence of the directional distribution of steel fibres on the mechanical anisotropy of 3D-printed concrete. It is worth noting that the orientation distribution of steel fibres exerts a remarkable impact on the mechanical properties of 3D-printed concrete.

Except for 3D printed concrete, alternative approaches have also been explored to investigate the influence of fibre distribution orientation on the mechanical properties of concrete. For instance, researchers have used many methods such as magnetic induction [24,25] and flow control [26,27] to manipulate the orientation of steel fibres. These studies collectively suggest that modifying the orientation of steel fibres in concrete can effectively alter the mechanical properties of SFRC. However, the existing research has primarily focused on inferring the impact of steel fibre orientation distribution on the macro-level mechanical properties of SFRC, especially 3D-printed SFRC, while lacking a comprehensive analysis of the underlying mechanisms involved. Therefore, it is imperative to establish a mesoscale perspective that elucidates the relationship between steel fibre orientation and mechanical properties in order to bridge this knowledge gap.

The purpose of this study was to investigate the effect of orientation distribution of steel fibres in 3D-printed SFRC on mechanical properties at hardened state. Firstly, the orientation distribution of steel fibres in 3D-printed concrete in previous studies was compared and analysed. Secondly, a three-dimensional mesoscale model was established for the first time to simulate the distribution and interaction of steel fibres in 3D-printed SFRC, and compares it with experimental results to verify the reliability of the model in analysing the impact of steel fibre orientation on SFRC performance. Finally, parameterized analysis was conducted using the verified mesoscale finite element model to explore the impact of steel fibres on the damage modes and mechanical properties of 3D-printed SFRC within different angle ranges by setting orientation angles η and θ. Through this study, it is possible to gain a clearer understanding of the impact of changes in steel fibre distribution on the mechanical properties of 3D-printed SFRC, thereby providing a theoretical basis for improving and controlling the performance of 3D-printed SFRC in future engineering applications.

2. Reviews of steel fibre distribution in 3D-printed concrete

It is well known that the fibres within fibre-reinforced concrete

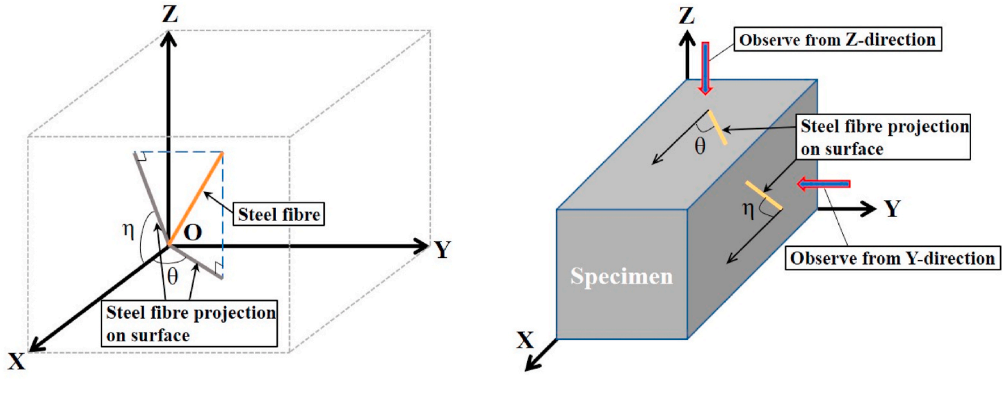

(a) Positioning of steel fibre (b) Observation direction

Fig. 1. Orientation angle positioning of steel fibre in concrete.

Table 1
Orientation distribution of steel fibres in other literatures.

Literature	Steel fibre length (mm)	Steel fibre volume (vol%)	Filament height size (mm)	Filament width size (mm)	Preparation method[a]	Steel fibre orientation angle (Approximate value)		
						0°–30°	30°–60°	60°–90°
Pham et al. [19]	3	1	6	10.5	MC	14 %	42 %	44 %
					3DP (η)	90 %	5 %	5 %
	6				MC	27 %	43 %	30 %
					3DP (η)	95 %	3 %	2 %
Arunothayan et al. [28]	6	1	10	10	3DP (θ)	94 %	6 %	0 %
		1		15	3DP (θ)	86 %	14 %	0 %
		1		20	3DP (θ)	75 %	25 %	0 %
		1		30	MC	26 %	49 %	25 %
		1		30	3DP (θ)	55 %	31 %	14 %
		2		30	MC	32 %	49 %	19 %
		2		30	3DP (θ)	77 %	21 %	2 %
		1		40	3DP (θ)	48 %	38 %	14 %
Zhou et al. [29]	6	4	15	20	MC	30 %	37 %	33 %
					3DP (η)	96 %	4 %	0 %
					3DP (θ)	70 %	23 %	7 %
Chen et al. [22]	12	2	50	50	MC	26 %	48 %	26 %
					3DP (η)	84 %	11 %	5 %
					3DP (θ)	93 %	6 %	1 %

[a] Note: In the preparation method, MC represents mould-casting, while 3DP denotes 3D-printing; θ and η in the brackets on the right of 3DP indicate the angle type between the observed projection and the X axis.

obtained through 3D printing are subjected to the constraints of the nozzle, resulting in an oriented distribution after extrusion. However, different printing parameters may lead to varying fibre orientations. To understand the mechanism of how the orientation distribution of steel fibres affects the performance of 3D-printed SFRC, it is necessary to firstly investigate the distribution of steel fibres within the concrete matrix. Therefore, this section summarizes the current research on steel fibre orientation in 3D-printed SFRC, with a focus on discussing the effects of steel fibre length, volume fraction, printing parameters, and nozzle shape on the orientation distribution of steel fibres.

The orientation of steel fibre can be described by its angle in three-dimensional space. In the existing research on 3D-printed steel fibre reinforced concrete, some scholars have detected the orientation distribution of steel fibre in 3D-printed concrete and mould-casted concrete by CT scanning. To compare and summarize the results of various literatures, the orientation angle of steel fibre was unified in this study, as shown in Fig. 1 (a). The orthogonal rectangular coordinate system is established, and the included angles between the projection of steel fibre on XOY plane and XOZ plane and X-axis were defined as θ and η, respectively. θ and η are acute angles, and the angle range is −90°~90°. The orientation of steel fibre can be determined by the angle of θ and η. In this study, it is uniformly stipulated that angle η was observed from the Y-direction and angle θ was observed from the Z-direction, as shown in Fig. 1 (b). Moreover, since the orientation and distribution of fibres in 3D-printed specimens are closely related to the printing direction, this study defines the X-direction as the printing direction of 3D-printed specimens. Table 1 summarizes the ratio of steel fibre content within the distribution range of different orientation angles in various literatures. It should be noted that in the summarized literature, the angles of θ and η are absolute values, that is, between 0°~90°. Pham et al. [19] obtained the ratio of steel fibre content in different angle η distribution ranges in their study; Arunothayan et al. [28] observed the ratio of steel fibre content in different angle θ distribution ranges; Zhou et al. [29] and Chen et al. [22] obtained the steel fibre content ratio in each distribution range of angle θ and η. The extrusion method studied by Chen et al. [22] is different from that of other scholars, which uses rectangular nozzle for horizontal extrusion, while other scholars use circular nozzle for vertical extrusion.

By comparing and observing the proportion of steel fibre in mould-casted concrete in Tables 1 and it is noted that the average proportion of steel fibre in 0°~30° range for 25.8 %, the average proportion of steel fibre in 30°~60° range for 44 %, and the average proportion of steel fibre in 60°~90° range for 30.2 %. For 3D-printed concrete, observing the distribution of steel fibres within each angle η range in different studies, it is found that when the round nozzle is utilized for vertical extrusion, the steel fibre content within the range of 0°~30° is greater than 90 %. For angle θ, with the increase in nozzle diameter, the proportion of steel fibre content in the range of 0°~30° gradually decreases, and the directivity begins to be inconspicuous. To sum up, the steel fibres in the fibre-reinforced concrete specimens obtained by 3D printing have evident directional distribution characteristics, and the degree of orientation has a great correlation with the nozzle size (print filament size). This can provide a way to control the distribution direction of steel fibres, and perhaps influence the mechanical properties of materials by regulating the orientation of steel fibres. However, the relationship between steel fibre orientation and mechanical properties has not been explored yet. To control mechanical properties through fibre orientation distribution, it is necessary to first clarify the changing relationship between the two.

3. Methodology of mesoscale modelling

Mesoscale finite element analysis is widely used to study the mechanical properties and damage mechanisms of concrete [30–32]. Currently, many studies have simulated the mechanical behaviour of SFRC at the mesoscale level and predicted its performance [33,34]. This study uses mesoscale finite element analysis to explore the impact of steel fibre orientation distribution on the performance of 3D-printed SFRC.

3.1. Generation of fibre model

In this study, the steel fibre model was generated by self-compiled program and ANSYS/LS-DYNA finite element software. The number of steel fibres generated was determined according to the space volume, fibre volume content, fibre diameter and fibre length. The specific process is shown in Fig. 2(a). The generation of steel fibre model was described in detail as follows.

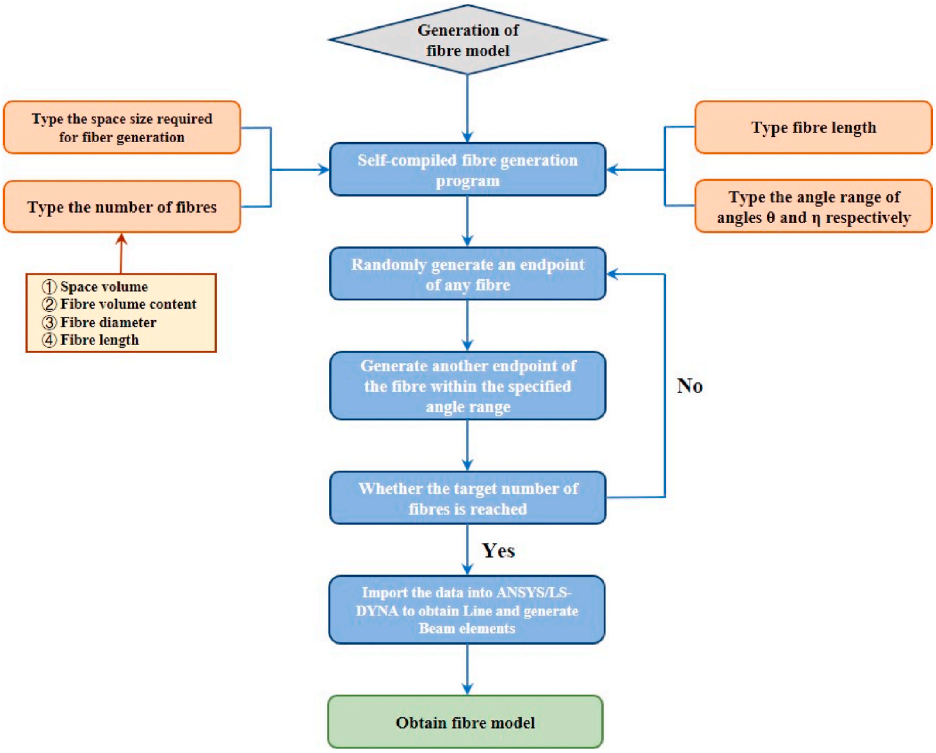

(a) Process

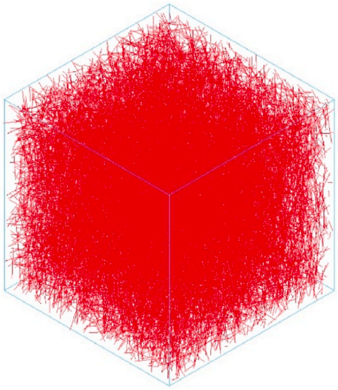

(b) Three-dimensional random mesoscale model

Fig. 2. Generation of fibre.

(a) Determine the basic information of generating steel fibre model, such as the generated steel fibre space volume (V_{sp}), the steel fibre volume content (C_{sf}), the steel fibre length (L_{sf}) and the steel fibre diameter (D_{sf});

(b) Determine the target number of steel fibres (N_{sf}). N_{sf} can be calculated by the parameters in Step (a), i.e., $N_{sf} = \frac{4V_{sp}C_{sf}}{\pi L_{sf} D_{sf}^2}$;

(c) Set the space size of the steel fibre generated, and the coordinates of each point in the space are (x, y, z);

(d) Generate an endpoint of a steel fibre at a random position in space;

(e) Generate the other endpoint of the steel fibre according to the steel fibre length and angle range (angle θ and η). When it is ensured that there is no steel fibre overlap, a steel fibre can be confirmed by two endpoints. Repeat Steps (c) and (d) until the target N_{sf} is reached, and obtain the steel fibre endpoint set file;

(f) Import the file in Step (e) into ANSYS/LS-DYNA, connect the data points in the endpoint set into lines, and then mesh the lines to obtain the steel fibre beam element model, as shown in Fig. 2(b).

3.2. Material model

In this study, LS-DYNA finite element software was used to analyse the influence of steel fibre orientation on the mechanical properties of SFRC [35].

The MAT_CONCRETE_DAMAGE_REL3 (MAT_072R3) model is a plasticity-damage model that represents an enhanced version of the K&C concrete model (Karagozian & Case local damage concrete model, is a material model that automatically generates parameters for concrete simulation, fully considering the strain rate effect, damage effect, strain strengthening and softening effect of concrete materials [36]), offering improved capabilities for prediction of the elastoplastic damage behaviour of concrete. This model utilizes three shear failure surfaces

Table 2
Parameters for determining the strength surfaces.

Symbol	a_{0m} (MPa)	a_{1m}	a_{2m} (MPa^{-1})	a_{1f}	a_{2f} (MPa^{-1})	a_{0y} (MPa)	a_{1y}	a_{2y} (MPa^{-1})
Value	44.341	0.446	0.000539	0.442	0.000789	33.48	0.625	0.001717

Table 3
The damage function values of λ – φ

λ	φ
0	0
0.000038	0.85
0.0001	0.95
0.00014	0.98
0.00024	1
0.00027	0.97
0.00039	0.79
0.00061	0.55
0.001	0.33
0.00165	0.17
0.0033	0.032
0.007	0.005
100	0

Table 4
Key input parameters of material models.

Parameter	Value
Mass density	7850 kg/m^3
Young's modulus	210 GPa
Poisson's ratio	0.3
Yield stress	2500 MPa

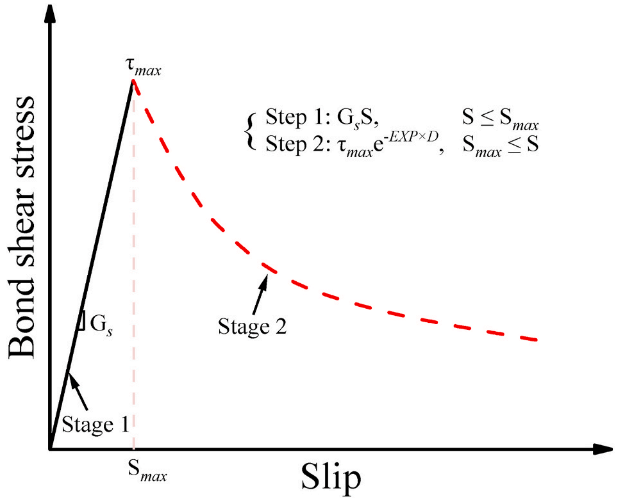

Fig. 3. Bond-slip curve between steel fibre and concrete matrix.

[37,38], namely the maximum yield surface ($\Delta\sigma_y$), maximum strength surface ($\Delta\sigma_m$), and residual strength surface ($\Delta\sigma_r$), which can be calculated from Eq. (1) ~ (3).

$$\Delta\sigma_y = a_{0y} + \frac{p}{a_{1y} + a_{2y}p} \tag{1}$$

$$\Delta\sigma_m = a_{0m} + \frac{p}{a_{1m} + a_{2m}p} \tag{2}$$

$$\Delta\sigma_r = a_{0f} + \frac{p}{a_{1f} + a_{2f}p} \tag{3}$$

where, p is the hydrostatic pressure, a-parameters are the user input, and for concrete, $a_{0f} = 0$. The current strength surface ($\Delta\sigma$), which is derived from $\Delta\sigma_y$, $\Delta\sigma_m$, and $\Delta\sigma_r$, can be calculated using Eqs. (4) and (5):

$$\Delta\sigma = \varphi(\lambda) \bullet \left(\Delta\sigma_m\text{-}\Delta\sigma_y\right) + \Delta\sigma_y \tag{4}$$

$$\Delta\sigma = \varphi(\lambda) \bullet \left(\Delta\sigma_m\text{-}\Delta\sigma_r\right) + \Delta\sigma_r \tag{5}$$

where, λ is the modified effective plastic strain; $\varphi(\lambda)$ is the interpolation function of λ. For the MAT_072R3 material model, the equation of state (EOS) needs to be input to express the relationship between hydrostatic pressure and volumetric strain. The modified EOS of SFRC can be found in Refs. [39,40]. Compared with other concrete material models, MAT_072R3 material model can capture the implicit constraints of reinforcement, which is very important to express the fibre effect in fibre reinforced concrete [41]. In this study, MAT_072R3 material model is used to simulate the performance of concrete matrix. The parameters used to determine the strength surface are shown in Table 2, The damage function of λ – φ is defined by 13 pairs. The full set (13 pairs) for UHPC is provided in Table 3 [42,43]. All concrete matrices in this study were UHPC, therefore the parameters in Tables 2 and 3 were applied to all concrete models.

MAT_PLASTIC_KINEMATIC (MAT_003) can describe isotropic hardening and follow-up hardening plastic models, and can also consider the effect of strain rate. It is suitable for beam, shell and solid elements, and has high calculation efficiency. Without considering the effect of strain rate, the radius of yield surface under this model is the initial yield strength plus the hardened part, as shown in Eq. (6):

$$\sigma_y = \sigma_0 + \beta E_p \varepsilon_{eff}^p \tag{6}$$

where, σ_y is the yield strength, σ_0 is the initial yield strength, E_p is the plastic hardening modulus, ε_{eff}^p is the effective plastic strain, β is a hardening parameter ($0 < \beta < 1$) to represent kinematic hardening. The plastic hardening modulus is given by the following equation:

$$E_p = \frac{E_t E}{E - E_t} \tag{7}$$

where, E is the elastic modulus and E_t is the tangent modulus. According to the difference of β value, it can be used to describe different hardening models: (1) when $\beta = 0$, it is follow-up hardening, the size of yield surface remains unchanged, and moves along the direction of plastic strain; (2) when $\beta = 1$, it is isotropic hardening, the position of yield surface remains unchanged, and the size changes with strain; (3) when $0 < \beta < 1$, it is mixed hardening. In this study, the MAT_003 material model is employed to simulate the properties of steel fibres. The specific key input parameters are shown in Table 4.

3.3. Constitutive laws of fibre-mortar interface

For SFRC, its mechanical properties are not only determined by the mechanical properties of the matrix, but also related to the reinforcement effect of steel fibre on the matrix. Steel fibre plays the role of limiting cracking, increasing ductility, and improving strength [44–46]. Therefore, a reasonable definition of the constitutive relationship between steel fibre and mortar interface can more accurately analyse the role of steel fibre in SFRC. At present, the coupling methods commonly used to define the interface constitutive relationship in LS-DYNA include setting common node and setting CONTACT_1D, and setting CONSTRAINED_BEAM_IN_SOLID, etc.

In this study, concrete matrix adopts solid element, steel fibre adopts

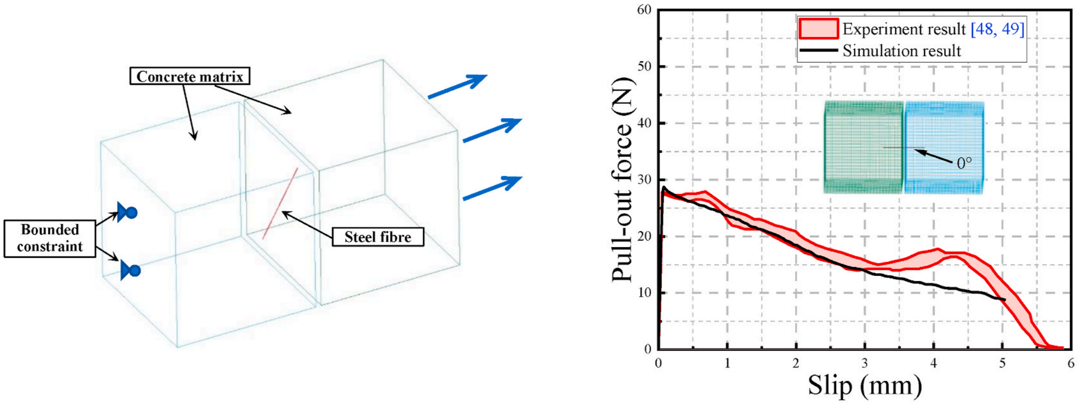

(a) Model setup of single fibre pull-out

(b) 0°

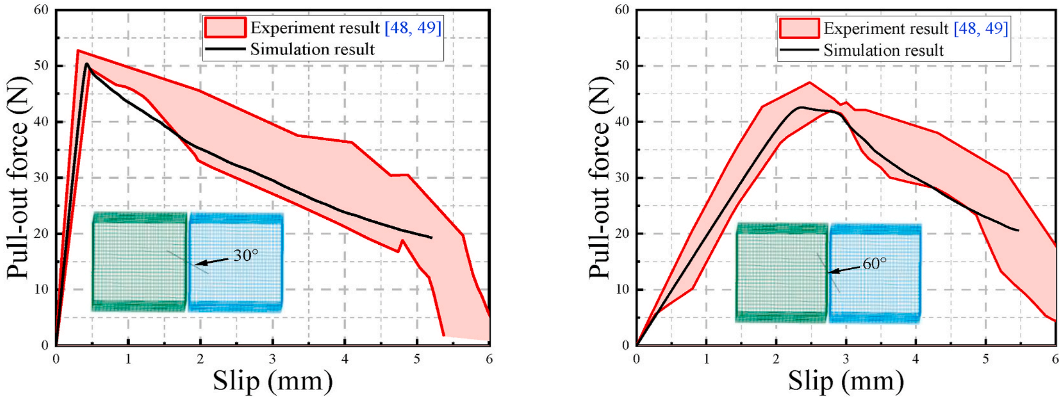

(c) 30°

(d) 60°

Fig. 4. Single fibre pull-out experiment and simulation results.

beam element, and setting CONSTRAINED_BEAM_IN_SOLID (CBIS) is used to define the bond between steel fibre and concrete. CBIS is an interaction mechanism developed on the basis of CONSTRAINED_LAGRANGE_IN_SOLID (CLIS) for fluid-solid coupling between models, which avoids some limitations in CLIS. This bond constraint model allows for the definition of the bond slip constitutive function between beam elements and solid elements, thereby achieving coupling between the two. In this study, the bond-slip constitutive relationship between steel fibre and concrete was established by DEFINE_FUNCTION. In this study, a simplified bond-slip constitutive model was used, which consists of two parts: the first part is the fully bonded and partially bonded stages, which are simplified as linear variations. The second part is the softening part, which corresponds to the complete debonding stage between fibres and concrete, and the interface force is purely provided by friction [41]. The bond-slip curve is shown in Fig. 3, where G_s is the bond shear modulus, D is the damage parameter, $\tau_{\max}$ is the bond shear stress, and $S_{\max}$ is maximum slip strain. The specific values can be obtained based on the experimental results using the calculation method provided by Su et al. [47]. The values of G_s, $\tau_{\max}$, and $S_{\max}$ determined in this study are 2.4×10^9 Pa, 1.48×10^7 Pa, and 3×10^{-3}, respectively. These parameters were used to define the bonding performance between all steel fibre models and concrete models in the following content.

In this study, the finite element simulation of single fibre pull-out is carried out and compared with the experimental results [48,49] to verify the accuracy of the coupling method between steel fibre and concrete matrix. Define the bond-slip relationship between steel fibres and concrete matrix based on experimental results [48,49] and input it into CONSTRAINED_ BEAM_ IN_ SOLID is used to define the interaction between steel fibres and concrete in simulation. Three fibre orientations were set in the experiment, which were 0°, 30°, and 60°, respectively. The size of steel fibre is 0.2 mm in diameter × 13 mm in length, and the size of concrete solid element on both sides is 25 mm × 25 mm × 25 mm, as shown in Fig. 4 (a). The comparison between simulation results and test data is presented in Fig. 4(b–d). It can be observed from the figure that the pull-out force and slip curve obtained by simulation are similar to the test results. The simulation results of the first stage are in the middle of the test error range, and their second stage is in the lower part of the test error range, but they are relatively close on the whole. Therefore, through the simulation results of single fibre pull-out, it can be considered that CONSTRAINED_BEAM_IN_SOLID simulation of the coupling between steel fibre and concrete matrix is reasonable.

4. Verification results and analysis

4.1. Control experiment

4.1.1. Specimen preparation and testing

To verify the accuracy of SFRC model of steel fibre directional distribution, 3D-printed SFRC specimens were prepared and tested to compare with the simulation results. Meanwhile, to make the material matrix structure as dense as possible, the 3D-printed SFRC material used in this study is actually 3D-printed ultra-high performance concrete (UHPC).

The 3D-printed SFRC specimen was fabricated using a desktop 3D printer (Fig. 5 (a)). The fabrication process involved initially mixing the materials thoroughly to obtain a homogeneous fresh mortar. The mixture proportion of fresh mortar is shown in Table 5. The fresh mortar was then placed into the material container of the 3D printer, and the printing process was initiated. During printing, the mortar was extruded

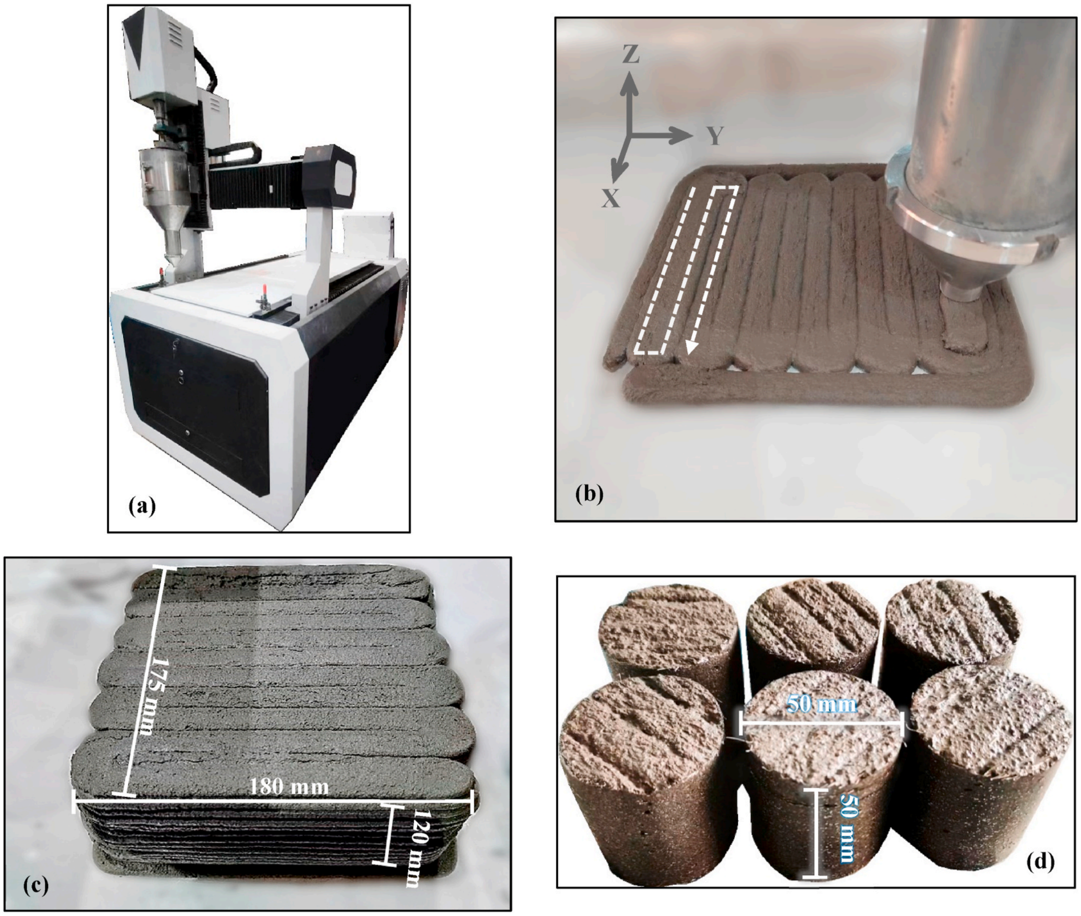

Fig. 5. (A) 3D printer (b) prints path (c) 3D-printed concrete block (d) 3D-printed specimen.

Table 5
3D-printed SFRC full mixture proportion (kg/m^3).

Cement	Silica fume	Fly ash	Quartz sand	NCC	Cellulose	PS	Water	Steel fibre
750	165	165	1080	24	1.08	10	154	78

Note: NCC represents nano calcium carbonate; PS represents polycarboxylate superplasticizer.

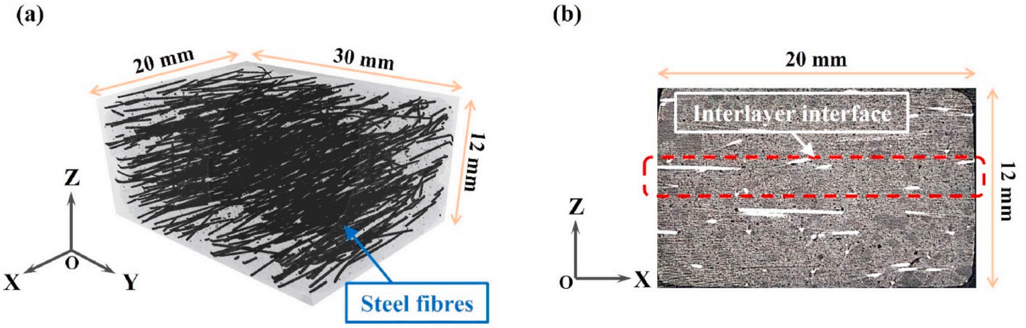

Fig. 6. CT scan results (a) steel fibres in 3D-printed SFRC specimens (b) matrix.

through the nozzle by the extruder, with the nozzle moving along the X-direction (the main printing direction) on the printing platform. Once the printing filament reached the desired length, it would move in the Y-direction before moving in the X-direction adjacent to the previously printed filament. This process was repeated until the desired length in the Y-direction was achieved. After completing one layer, the printing process would move to the Z-direction and repeat the printing of the previous layer, as depicted in Fig. 5 (b). The printer utilized a round-shaped nozzle with a diameter of 15 mm. The speed at which the mortar is extruded was set to 5 mm/s, and the speed at which the nozzle moves was 15 mm/s. By printing layer by layer, a 3D-printed test block measuring 180 mm × 175 mm × 120 mm was obtained, with each layer having a height of 6 mm, as shown in Fig. 5 (c). Following the printing, the test block was cured at ambient temperature for 28 days.

Table 6
Proportion of steel fibre content in different orientations in 3D-printed SFRC.

Angle number	Proportion of steel fibre content		
	0°–30°	30°–60°	60°–90°
θ	86 %	14 %	0 %
η	95 %	5 %	0 %

Subsequently, the 3D-printed test block was cut and cored to obtain cylindrical specimens with dimensions of 50 mm × 50 mm (diameter × height) (Fig. 5 (d)), which were then subjected to compressive and splitting tensile tests.

In the test, the steel fibre used to prepare SFRC was copper plated round straight steel wire with a diameter of 0.12 mm and a length of 6 mm. Its ultimate tensile strength is large than 2500 MPa. The volume content of these steel fibres in SFRC is 1 vol%.

This study reconstructed the distribution of steel fibres in the aforementioned 3D-printed SFRC specimens through CT scanning, as indicated in Fig. 6. During the CT scan, the Source-to-Object Distance (SOD) is set to 211.96 mm, and the Source-to-Detector Distance (SDD) is set to 591.96 mm. The voxel resolution was set to 0.0716mm/voxel. The sample under measurement was cut from a 3D-printed test block and has dimensions of 30 mm × 20 mm × 12 mm. To ensure the accuracy of the results, CT scans were performed on samples cut at three different positions. From Fig. 6 (a), it can be seen that steel fibres have obvious directional characteristics in the matrix. The distribution of orientation angles of various steel fibres in the CT scan images was summarized, and the steel fibre content in the range of angles θ and η of steel fibres in 3D-printed SFRCs was obtained within different ranges. The proportion of steel fibre content in different orientations is listed in Table 6. In addition, by observing Fig. 6 (b), it can be observed that the 3D-printed specimen matrix in this experiment is relatively dense, with almost no defects at the interlayer interface, and the printing quality is good.

4.1.2. Loading method

Given the anisotropy of 3D-printed SFRC due to the directional distribution of steel fibres, it becomes imperative to assess its mechanical properties across various directions. In this study, an orthogonal rectangular coordinate system was established, aligned with the print path, to define the loading directions precisely. Concretely, the X-direction aligns with the print direction, whereas the Z-direction is perpendicular to the print surface, as clearly depicted in Fig. 7. To comprehensively evaluate the mechanical properties, the compressive strength was determined by conducting axial compression tests on cylindrical specimens. For instance, to obtain the compressive strength in the X-direction, specimens were cored along the X-axis and loaded in the same direction. Analogous procedures were followed for the Y- and Z-directions. Additionally, tensile strength was measured through splitting tension tests on cylindrical specimens. Here, the tensile strength in the X-direction was determined by coring along the Z-direction and applying a load in the Y-direction. Similarly, the tensile strength in the Y-direction was measured by coring along the X-direction and loading in the Z-direction, and the tensile strength in the Z-direction was measured by coring along the Y-direction and loaded in the X-direction, as schematically shown in Fig. 7. To maintain consistency between simulations and experiments, the coordinate system and load direction same as

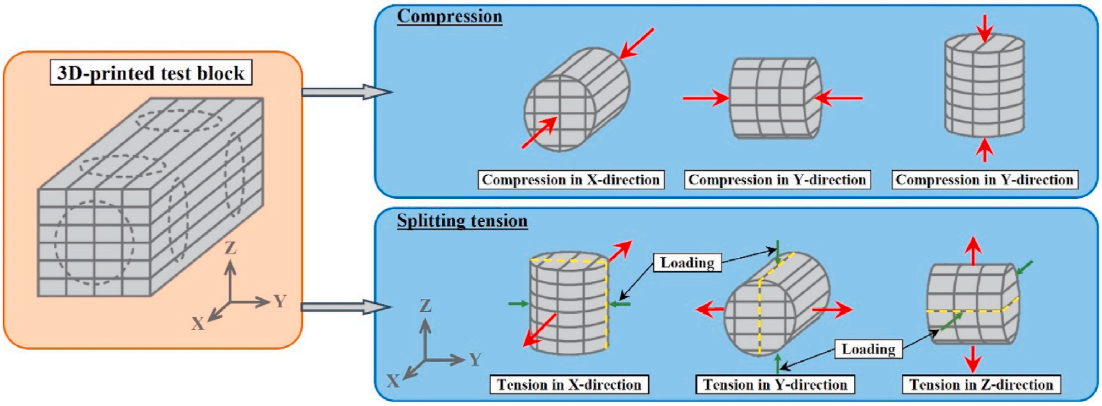

Fig. 7. Loading setting method of compression and splitting tension.

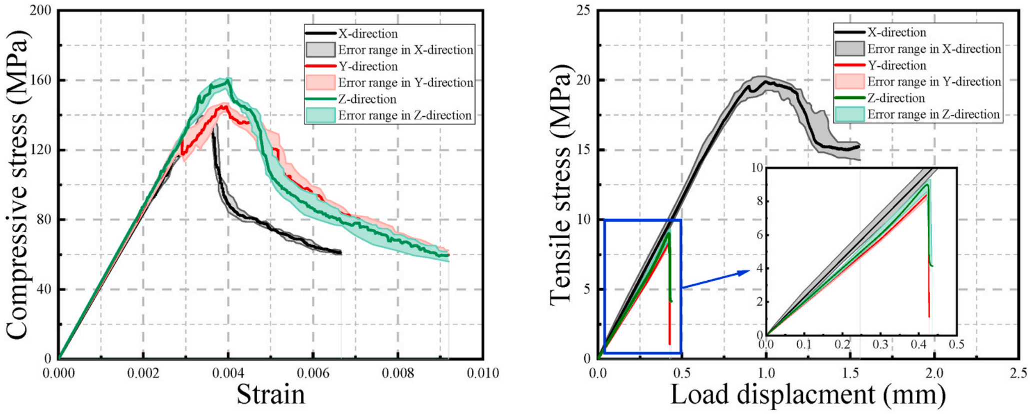

(a) Compressive stress (c) Tensile stress

Fig. 8. Compression and tension test results.

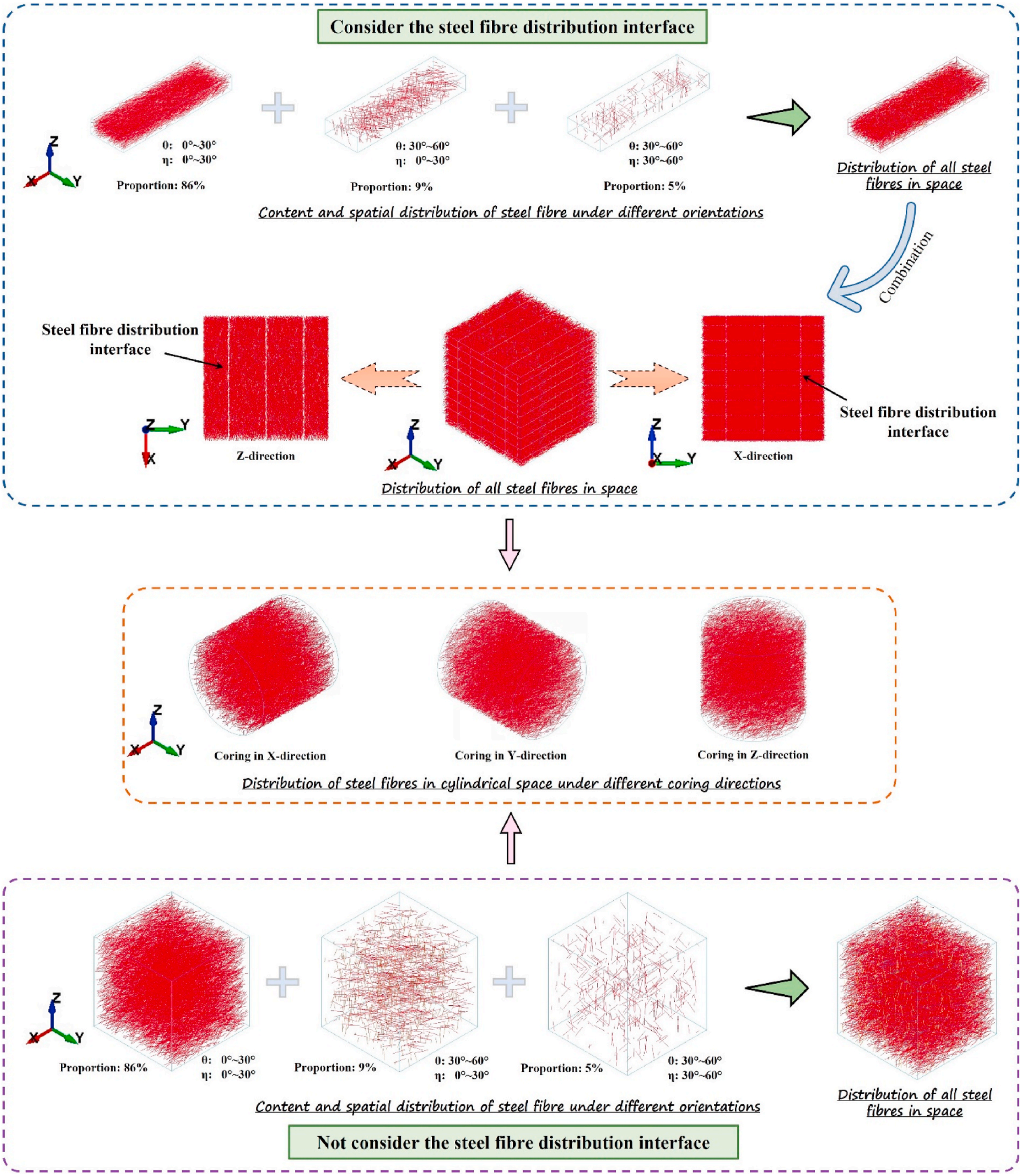

Fig. 9. The steel fibre generation process in the verified model.

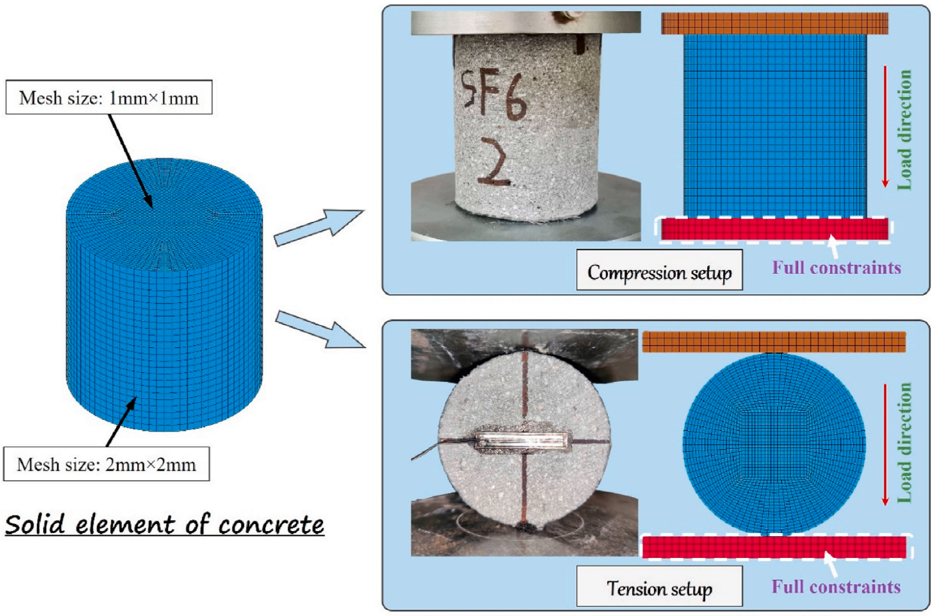

Fig. 10. Meshing and loading settings.

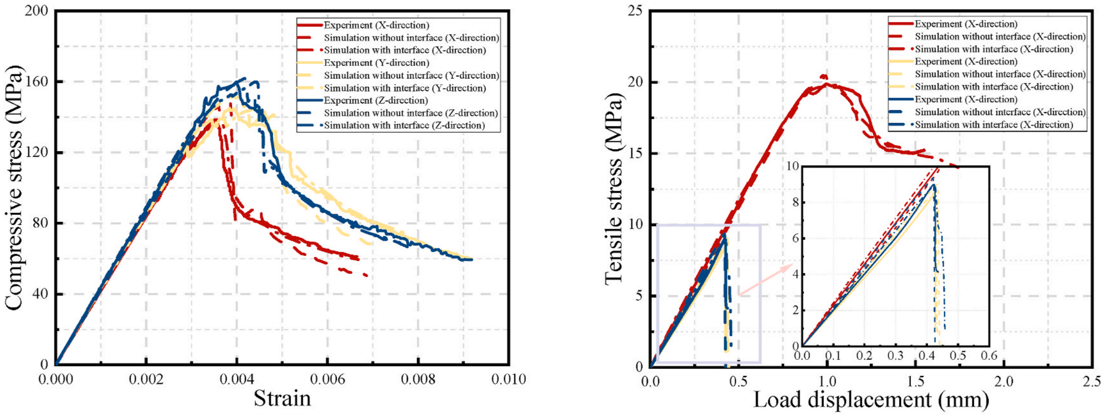

(a) Compression

(b) Tension

Fig. 11. Comparison of mechanical results between experiment and simulation.

experiment were adopted in the subsequent simulations.

4.1.3. *Test result*

Through the test method described in Section 4.1.2, the compressive and tensile strength of 3D-printed SFRC specimens were obtained, as shown in Fig. 8. Under the steel fibre distribution state described in Section 4.1.1, the average compressive strength of 3D-printed SFRC in the X-, Y- and Z-directions is 138.54 MPa, 144.98 MPa, and 159.92 MPa, respectively; while the average tensile strength of 3D-printed SFRC in the X-, Y- and Z-directions is 19.89 MPa, 8.51 MPa, and 8.99 MPa, respectively. Through the test, it is noted that the compressive and tensile strengths of 3D-printed SFRC with directional distribution of steel fibres exhibit anisotropic characteristics. Moreover, it can be observed that the orientation of steel fibre has a great influence on the ductility of SFRC. As SFRC is tensioned along the steel fibre distribution direction (X-direction), it exhibits ductile damage, while as SFRC is tensioned perpendicular to the steel fibre distribution direction (Y- and Z-direction), it demonstrates brittle damage.

4.2. *Establishment of mesoscale models*

Based on the above test results, the mesoscale finite element modelling was carried out, and the compressive and tensile behaviour in different directions was simulated. The simulation results were compared with the experimental data to verify the accuracy of the established mesoscale 3D-printed SFRC model. It is worth mentioning that the 3D-printed SFRC matrix used in the experiment is dense without interlayer defects, as shown in Fig. 6. This study aims to investigate the effect of fibre orientation on 3D-printed SFRC, and therefore, the bonding interface between printed filaments was not considered in the establishment of the concrete matrix model. However, due to the layer-by-layer printing method, the steel fibres in 3D-printed SFRC were confined within each 3D-printed filament, which means that the steel fibres hardly cross the bonding interface between 3D-printed filaments. This results in an interface formed by the fibre distribution at the bonding interface. Therefore, when validating the model, fibre model needs to take into account this distribution. Moreover, a model without the steel fibre distribution interface was established as a control group.

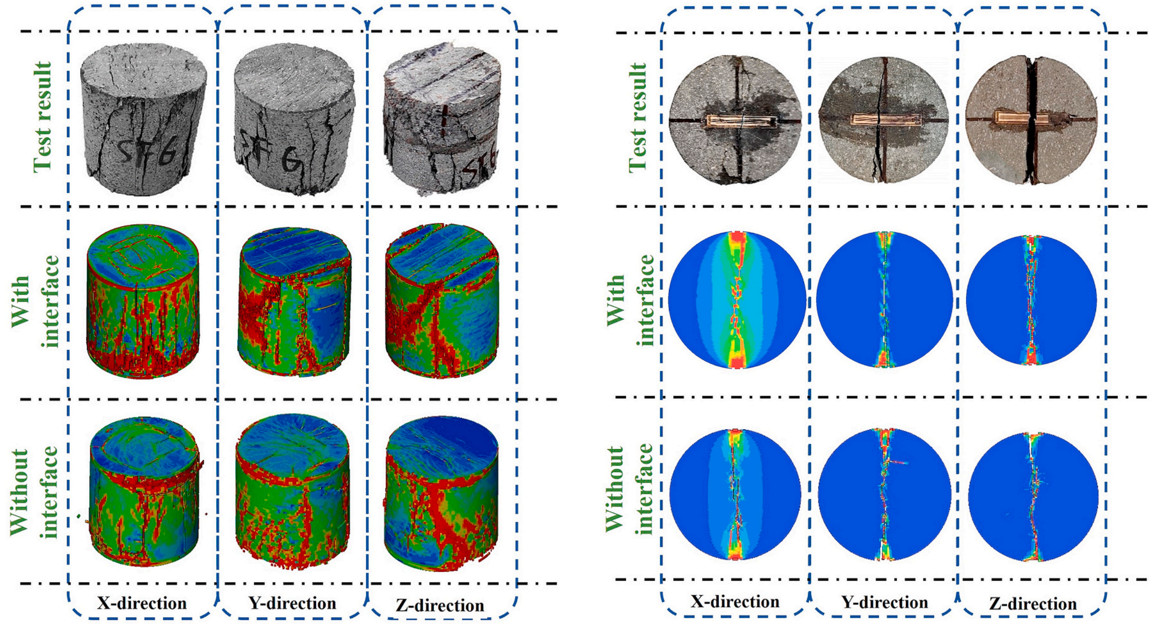

(a) Compression (b) Tension

Fig. 12. Comparison of failure models between experiment and simulation.

The establishment process of mesoscale SFRC model is as follows.

With steel fibre distribution interface:

Step 1: Through the self-compiled program, the fibre beam element model was generated within the cube space range of 6 mm × 15 mm × 50 mm. Among them, the steel fibre content with the angle θ between −30°–30° and the angle η between - 30°–30° accounts for 86 % of the total content; the steel fibre content with angle θ between −30° and −60° and 30°–60° and angle η between −30°–30° accounts for 9 % of the total content; the steel fibre content with angle θ between −30° and −60° and 30°–60° and angle η between −30° and −60° and 30°–60° accounts for 5 % of the total content. The fibre spatial distribution of each content ratio is shown in Fig. 9. Finally, merge the steel fibre beam element models of the three ranges into one fibre model.

Step 2: The steel fibre beam element model in the single 3D-printed filament established in Step 1 was combined in the layer-by-layer stacking manner as in the experiment, and then a total steel fibre beam element model in cubic space range size of 50mm × 50mm × 50 mm was obtained, as shown in Fig. 9.

Step 3: Core the cube space range in the Step 2 from X-, Y-, and Z-directions, respectively (consistent with the test construction method), and only the steel fibre beam element model within the cylindrical space range with a diameter of 50 mm and a height of 50 mm was reserved, as shown in Fig. 9.

Without the steel fibre distribution interface:

Step 4: Through the self-compiled program, the fibre beam element model was generated within the cube space range of 50 mm × 50 mm × 50 mm. Among them, the steel fibre content same as Step 1. The fibre spatial distribution of each content ratio is shown in Fig. 9.

Step 5: Same as Step 3, Core the cube space range in the Step 4 from X-, Y-, and Z-directions, respectively, and only the steel fibre beam element model within the cylindrical space range was reserved, as shown in Fig. 9.

Step 6: Concrete adopts solid element model. According to the experimental requirements, the concrete model is a cylinder with a diameter of 50 mm and a height of 50 mm, as shown in Fig. 10. The concrete model is composed of a fully integrated hexahedral solid element mesh, and the steel fibre adopts a beam element. The mesh size outside the cylinder is 2 mm × 2 mm, the minimum mesh size inside is about 1 mm × 1 mm. The model consists of a total of 502887 nodes and 460026 elements. As described in Section 3.3, the concrete model and steel fibre model adopt CONSTRAINED_BEAM_IN_SOLID coupling mode. The compression and tension settings of the SFRC mesoscale model are consistent with the test. The algorithm in this study adopts display algorithm, and the effect of strain rate is not considered in the material model.

4.3. *Comparison and verification of experiment and simulation results*

To verify the accuracy of the simulation results, the foregoing test data were compared with simulation results, and the strength change laws of compression and tension are illustrated in Fig. 11. Fig. 11 (a) presents the compressive stress–strain curve of the test and simulation. By comparison, it can be found that the stress-strain curve of the model with the distribution interfaces of steel fibres is close to the experimental results, while the simulation results without interfaces were slightly higher than the experimental results. The reason for this difference may be due to the presence of steel fibre distribution interfaces. A specimen with interfaces forms weak surfaces at the interface, while a specimen without an interface don't have a weak surface [15,50,51]. However, despite the differences, the stress differences in the X, Y, and Z directions are not significant, only 6.8 %, 5.0 %, and 1.2 %, respectively, and the anisotropic characteristics are the same. Fig. 11(b) presents the curve of tensile stress–loading displacement tested and simulated. Through comparison, it was found that both types of simulation results were closer to the experimental results, and the three exhibited the same directional dependence.

Besides, the failure of test and simulated test pieces is compared in Fig. 12. It is noted from the figure that the failure modes of concrete in the test and simulation are similar, which indicates that this model can well reflect the failure of SFRC. The confinement effect of steel fibre on concrete in the simulation is the same as that of steel fibre on concrete matrix in the actual specimen.

To sum up, by comparing the test data with the simulation results, it can be judged that the aforementioned simulation method can accurately reflect the effect of steel fibre orientation on SFRC. Therefore, the influence mechanism of steel fibre orientation distribution on the mechanical properties of 3D-printed SFRC can be analysed parametrically using this method. Besides, the simulation results clearly indicate that the orientation distribution of steel fibres is the primary reason for the direction-dependent characteristics of 3D-printed SFRC. Therefore, to gain a more comprehensive understanding of the impact of steel fibre orientation changes on the performance of 3D-printed SFRC, a parameter analysis is conducted with the steel fibre orientation range as the variable. Considering that the results with and without fibre interfaces

Table 7
Fibre distribution parameters of finite element analysis group.

Group	Distribution interval of angle		Spatial distribution range of single steel fibre	The orientation of steel fibres in space was observed from different directions		
	η (°)	θ (°)		X-direction	Y-direction	Z-direction
G-1-0-0	0°~0°	0°~0°	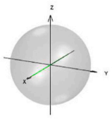	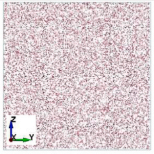	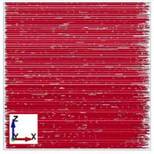	
G-2-30-0	-30°~30°	0°~0°	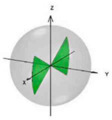	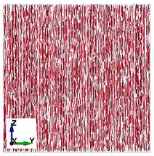	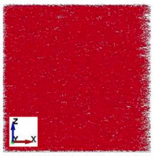	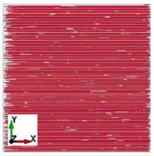
G-3-30-30	-30°~30°	-30°~30°	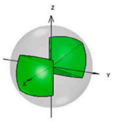	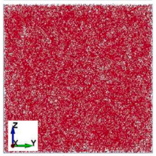	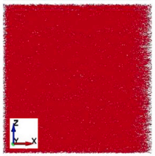	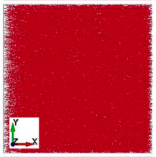
G-4-60-0	-60°~60°	0°~0°	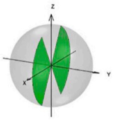		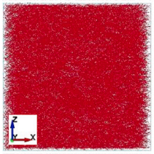	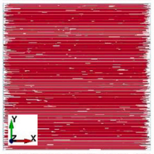
G-5-60-30	-60°~60°	-30°~30°	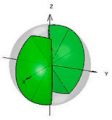	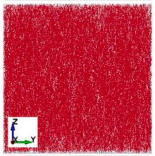	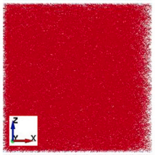	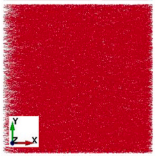
G-6-60-60	-60°~60°	-60°~60°	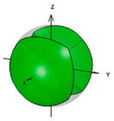	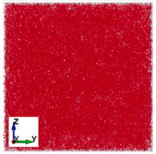	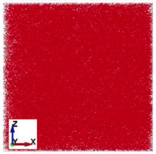	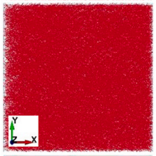
G-7-90-0	-90°~90°	0°~0°	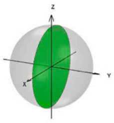	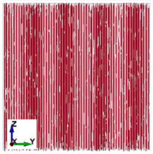	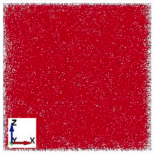	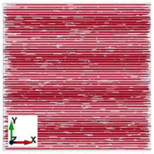
G-8-90-30	-90°~90°	-30°~30°	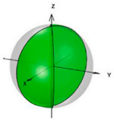	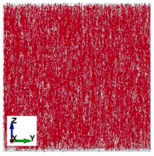	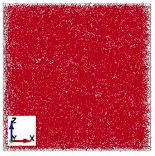	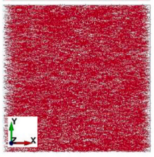
G-9-90-60	-90°~90°	-60°~60°	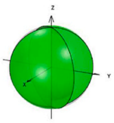	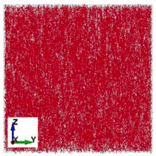	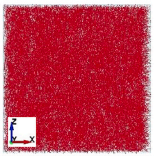	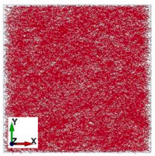
G-10-90-90	-90°~90°	-90°~90°	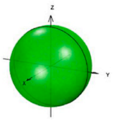	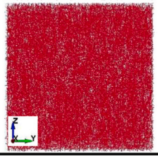	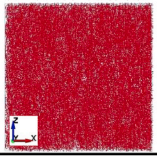	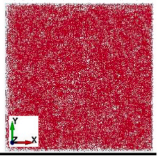

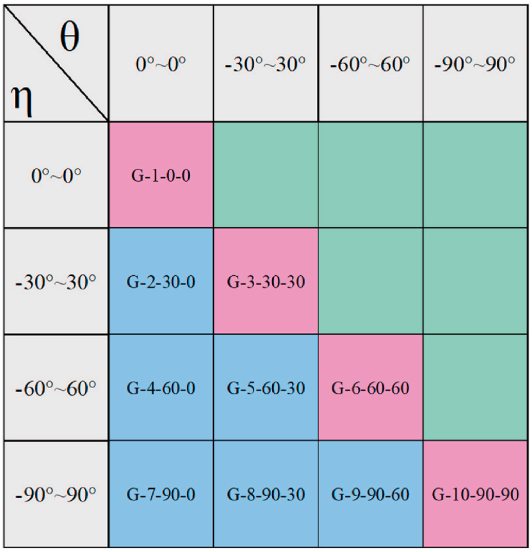

η \ θ	0°~0°	-30°~30°	-60°~60°	-90°~90°
0°~0°	G-1-0-0			
-30°~30°	G-2-30-0	G-3-30-30		
-60°~60°	G-4-60-0	G-5-60-30	G-6-60-60	
-90°~90°	G-7-90-0	G-8-90-30	G-9-90-60	G-10-90-90

Fig. 13. The relationship between the selection of specimens and the orientation angle of steel fibres.

are similar and to avoid interference from other factors, the distribution interface of steel fibres is not considered in the parameter analysis.

5. Parametric study

The influence of steel fibre distribution direction on the mechanical properties and damage modes of 3D-printed SFRC is studied based on the 3D mesoscale model verified above. In this study, ten control groups were designed according to the angles η and θ of steel fibre (Table 7), i.e. when η and θ are both 0°; η is in the range of −30°–30° and θ is 0°; η is in the range of −30°–30° and θ is in the range of −30°–30°; η is in the range of −60°–60° and θ is 0°; η is in the range of −60°–60° and θ is in the range of −30°–30°; η is in the range of −60°–60° and θ is in the range of −60°–60°; η is in the range of −90°–90° and θ is 0°; η is in the range of −90°–90° and θ is in the range of −30°–30°; η is in the range of −90°–90° and θ is in the range of −60°–60°; η is in the range of −90°–90° and θ is in the range of −90°–90°. Among them, when the angular distribution range of η and θ is −90°–90°, it indicates that the steel fibres are randomly distributed in space. It is worth noting that as the range of angles η and θ changes, the damage and mechanical properties in the Y and Z-directions exhibit oblique symmetry (as shown in Fig. 13), such as, when the orientation angles η and θ of steel fibres are distributed between −60°–60° and −30°–30°, the mechanical properties and damage of the specimen in the Y-direction are consistent with those in the Z-direction when the orientation angles η and θ of steel fibres are distributed between −30°–30° and −60°–60°, respectively. Similarly, the performance of the former in the Z-direction is the same as that of the latter in the Y-direction, while the X-direction performance is consistent with both. Therefore, only one case is considered in this study.

In order to facilitate understanding, ten control groups were numbered in the form of G-A-B-C, where A represents the group number, including 1 to 10; B denotes the maximum angle that angle η can reach, which can be 0, 30, 60, and 90 respectively; C refers to the maximum angle that angle θ can reach, and 0, 30, 60, and 90 can be taken, respectively.

5.1. *Local damage of concrete*

5.1.1. *Compression*

Table 8 comprehensively details the compression damage nephograms observed in various specimen types loaded in distinct directions. It can be found that the fibre orientation plays a pivotal role in determining the damage mode exhibited by the specimen. Specifically, When the orientation angles η and θ of the fibres are both 0°, the specimen G-1-0-0 loaded in the X-direction exhibits a characteristic annular damage nephogram, whereas in the Y- and Z-directions, parallel through cracks are evident. As the range of angle η broadens while angle θ remains fixed at 0°, specimens G-2-30-0 and G-4-60-0 loaded in the X-direction continue to exhibit annular damage nephograms. However, as the angle range widens, the annular damage pattern becomes increasingly less obvious. This annular damage is primarily attributed to the emergence of circumferential horizontal tension within the concrete specimen during compression. For instance, in G-1-0-0, as depicted in Fig. 14 (a, b), the directional distribution of internal steel fibres aligned with the X-direction precludes them from effectively constraining circumferential cracking within the specimen. Conversely, when the range of η encompasses −90°–90°, specimen G-7-90-0 loaded in the X-direction ceases to exhibit annular damage and instead manifests through transverse cracks. Besides, the damage model of G-7-90-0 loaded in the Z-direction is the same as that in the X-direction. This behaviour is primarily due to the presence of horizontally or nearly horizontally aligned steel fibres within the specimen as the η angle range widens to −90°–90°. When the specimen undergoes lateral deformation under the influence of horizontal tension, it is restrained by steel fibres aligned along the Z-direction, effectively limiting crack propagation, as evident in Fig. 14 (c, d).

Moreover, for G-1-0-0, G-2-30-0, G-4-60-0, and G-7-90-0, several cracks parallel to the XOZ plane appeared in the specimen when loaded along the Y-direction. This is mainly because the angle θ of the steel fibres in these specimens is 0°. In this case, the distribution of steel fibres is parallel to the XOZ plane, which causes the steel fibres in SFRC to form a ‘layered’ feature, lacking constraints in the Y-direction. As the range of angle θ increases, cracks parallel to the XOZ plane in the specimen ‘disappear’ when loaded in the Y-direction.

Overall, steel fibres in 3D-printed SFRC have a significant impact on the compression damage mode of 3D-printed SFRC. By adjusting the orientation of steel fibres, the compression damage mode of SFRC can be regulated.

5.1.2. *Tension*

As compared to compressive damage, the tensile damage of 3D-printed SFRC is more significantly affected by the directional distribution of steel fibres, which is mainly related to the steel fibres providing tensile direction constraints in concrete. Table 9 presents the tensile damage modes of different groups of specimens under different loading directions. When the values of angles η and θ are 0°, it is evident that the steel fibres in G-1-0-0 only provide tensile force in the X-direction. From Tables 9 and it can be observed that when G-1-0-0 is subjected to tension in the X-direction, the distribution range of the equivalent strain nephogram of the specimen is large. However, when G-1-0-0 is subjected to tension in the Y- and Z-directions, failure and cracking occur in the middle of the specimen. This indicates that the steel fibres provide constraints in the X-direction for the specimen to produce ductile damage, while the Y- and Z-directions do not provide constraints.

For specimens G-2-30-0, G-4-60-0, and G-7-90-0, significant cracking occurs in the Y-direction when subjected to tension, mainly owing to the fact that the angle η in the specimen is 0° and SFRC is not constrained by steel fibres in the Y-direction. But in the Z-direction, combined with G-1-0-0, the damage between these specimens exhibits significant differences. When $\theta = 0°$, SFRC breaks into two parts after being subjected to ultimate load; when $-30° \leq \theta \leq 30°$, SFRC cracks in the middle, but does not clearly separate into two parts; when $-60° \leq \theta \leq 60°$, and SFRC is subjected to tension along the Z-direction, the strain region in the concrete matrix increases, but mainly concentrated at the upper and lower ends of the compression; when $-90° \leq \theta \leq 90°$, the tensile strain region of SFRC in the Z-direction significantly expands, exhibiting overall ductile damage. Fig. 15 displays the axial stress nephograms of the steel fibres inside the specimens G-1-0-0, G-2-30-0, G-4-60-0, and G-7-90-

Table 8
Compressive damage nephogram.

Group	Distribution interval of angle		The compressive damage nephogram was observed from different directions		
	η (°)	θ (°)	X-direction	Y-direction	Z-direction
G-1-0-0	0°~0°	0°~0°	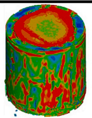	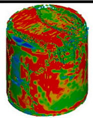	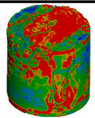
G-2-30-0	-30°~30°	0°~0°	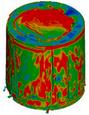	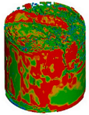	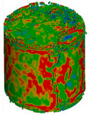
G-3-30-30	-30°~30°	-30°~30°	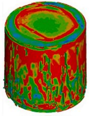	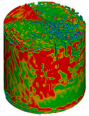	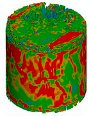
G-4-60-0	-60°~60°	0°~0°	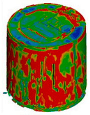	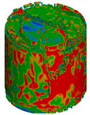	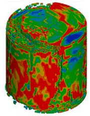
G-5-60-30	-60°~60°	-30°~30°	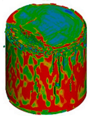	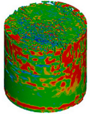	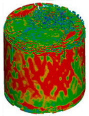
G-6-60-60	-60°~60°	-60°~60°	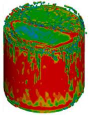	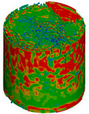	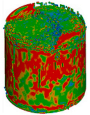
G-7-90-0	-90°~90°	0°~0°	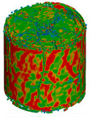	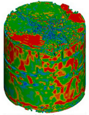	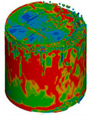
G-8-90-30	-90°~90°	-30°~30°	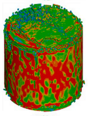	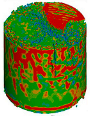	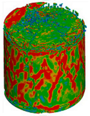
G-9-90-60	-90°~90°	-60°~60°	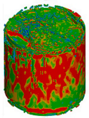	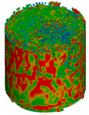	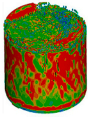
G-10-90-90	-90°~90°	-90°~90°	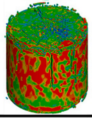	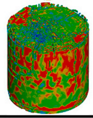	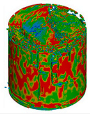

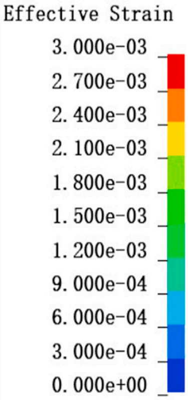

0 during tension along the Z-direction. When G-1-0-0 cracks, owing to the fibre distribution direction parallel to the crack direction, the axial stress of the fibres in the specimen is almost zero, and only a few fibres at the crack have axial stress; the presence of fibres with axial stress during cracking at G-2-30-0 has increased compared to G-1-0-0, but the overall number is still relatively small; unlike the previous two, the number of fibres with axial force in the middle of G-4-60-0 increases, and there are still compressed fibres at the upper and lower ends of the specimen after cracking, indicating that the specimen is still subjected to loading at the upper and lower ends after cracking without overall cracking. This phenomenon indicates that there is steel fibre limiting the failure of the overall specimen at this time, so that SFRC does not undergo brittle failure after cracking; for G-7-90-0, the number of tensile steel fibres significantly increased after the specimen cracked, and there were also compressive steel fibres at the upper and lower ends, indicating that G-7-90-0 still provides bearing capacity after cracking. This is mainly attributed to the constraint effect of steel fibres on the concrete matrix, which prevents SFRC experience brittle damage but rather ductile damage [52]. Moreover, it is noted from Fig. 15 that for G-1-0-0 and G-2-30-0, there were only compressed steel fibres and no tensile steel fibres during the loading process prior to cracking. For G-7-90-0, prior to the specimen cracks, the steel fibres in the middle section that are nearly parallel to the tensile direction were subjected to tension. The presence of these fibres delays the cracking of the matrix, thereby providing assistance in improving strength.

Considering symmetry, when G-7-90-0, G-8-90-30, G-9-90-60, and G-10-90-90 are subjected to tension in the Y-direction, the stress situation of the steel fibre is the same as the above results.

Overall, when the distribution direction of steel fibres is perpendicular to the tensile direction or the angle between the distribution direction of steel fibres and the tensile direction is greater than 60°, the limiting effect of steel fibres on concrete cracking is relatively low and

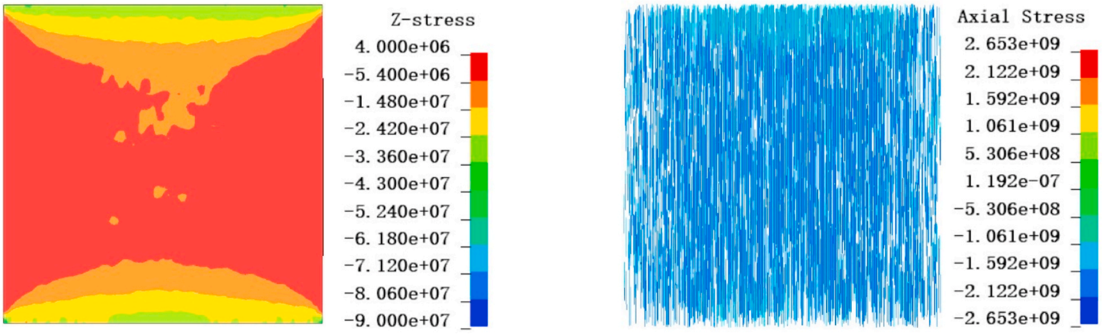

(a) Horizontal stress nephogram of G-1-0-0 (b) Fibre axial force nephogram of G-1-0-0

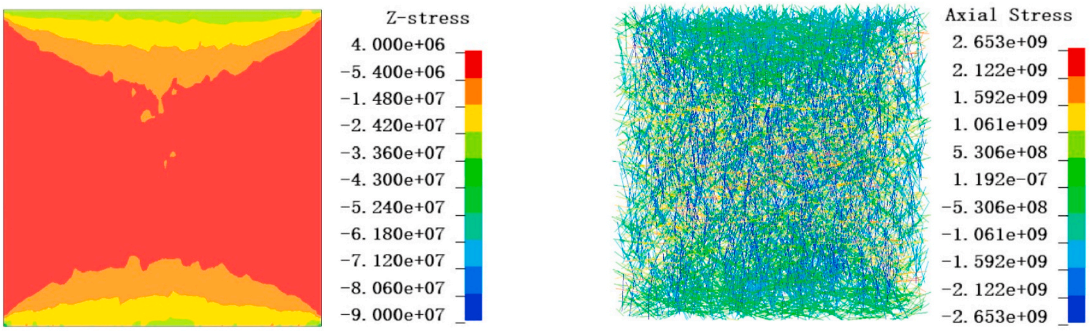

(c) Horizontal stress nephogram of G-7-90-0 (d) Fibre axial force nephogram of G-7-90-0

Fig. 14. Comparison of stress nephograms between G-1-0-0 and G-7-90-0 (Unit: Pa).

cannot cause ductile damage to 3D-printed SFRC. However, when there are many steel fibres with an angle less than 60°, they can induce ductile damage to SFRC. Therefore, the orientation of steel fibres has a decisive impact on the damage mode of 3D-printed SFRC.

5.2. *Peak stress of SFRC*

From Section 5.1, it can be seen that the orientation change in steel fibres impacts the internal stress of steel fibres in the specimen, which results in different damage modes in 3D-printed SFRC. Similarly, owing to the different stress situations of steel fibres with different orientations in 3D-printed SFRC, this has an impact on the overall stress of 3D-printed SFRC. The influence of fibre orientation on compressive and tensile mechanical properties is analysed below.

5.2.1. *Compression*

Compressive simulations were conducted on specimens of different groups and compressive strength was obtained. The test results are listed in Table 10. Referring to the symmetry in Figs. 13 and 16 summarizes the data values in Table 10 and the symmetric data values, demonstrating the variation in compressive strength with changes in fibre orientation. It should be noted that the angle values in the figure represent a range, that is, in Fig. 16, the angle η is 90° represents $-90^\circ \leq \eta \leq 90^\circ$. Fig. 16(a) shows the variation in compressive strength in X-direction. It can be seen that the strength is the highest when both the angles η and θ are 0°. As the angle range increases, the compressive strength in the X-direction initially decreases and then increases. Comparing Fig. 16 (b) and (c), it can be observed that the relationship between the compressive strength of the specimen and the fibre orientation angle is similar in the Y- and Z-directions. But the symmetry as shown in Fig. 13, when the same strength is achieved in the Y and Z directions, the values of angles η and θ are exactly opposite. For example, the compressive strength in the Y-direction when $\eta = 0^\circ$ and $-30^\circ \leq \theta \leq 30^\circ$ is the same as the compressive strength in the Z-direction when $-30^\circ \leq \eta \leq 30^\circ$ and $\theta = 0^\circ$. This phenomenon is mainly related to the symmetry of fibre distribution in orthogonal rectangular coordinate system.

The impact of steel fibre orientation on the strength of 3D-printed SFRC is readily apparent. Fig. 17 illustrates this influence by examining two aspects: "one angle range remains unchanged while the other angle range increases" and "both angle ranges increase together". In Fig. 17 (a), the changes in SFRC strength in all directions are depicted as the range of angle η increases while angle θ remains at 0°. It is evident that 3D-printed SFRC exhibits clear mechanical anisotropy characteristics. Specifically, the compressive strength of SFRC in the X-direction initially decreases (from 171.0 MPa to 149.5 MPa) and then increases (from 149.5 MPa to 152.6 MPa) as the angle η range increases. This phenomenon may be attributed to the compression and tension behaviour of steel fibres in specimen during loading. For specimen G-1-0-0, the angles η and θ are both 0°. At this time, all the steel fibres provide compressive bearing capacity for the specimen, thus achieving the highest compressive strength of the specimen. As the range of angle η increases, the number of fibres under pressure decreases, and there is no steel fibre that provides lateral tension in the horizontal direction, resulting in a decline in strength. From Fig. 14, it is apparent that there are steel fibres providing horizontal constraints in specimen G-7-90-0, which is also the reason why the strength of SFRC in the X-direction rises again when $-90^\circ \leq \eta \leq 90^\circ$. For the Y-direction, the compressive strength of SFRC gradually increases with the angle η range. The maximum value is achieved when $-90^\circ \leq \eta \leq 90^\circ$, and the compressive strength is 4.06 % higher than when $\eta = 0^\circ$. For the Z-direction, the compressive strength of SFRC gradually decreases with the increase in the angle η range. The minimum value is obtained when $-90^\circ \leq \eta \leq 90^\circ$, and the compressive strength decreases by 5.10 % as compared to $\eta = 0^\circ$. This indicates that an increase in the horizontal orientation angle range enhances the compressive strength of 3D-printed SFRC, while an increase in the vertical orientation angle range reduces the compressive strength of 3D-printed SFRC.

Table 9
Tensile damage nephogram.

Group	Distribution interval of angle		The tensile damage nephogram was observed from different directions		
	η (°)	θ (°)	X-direction	Y-direction	Z-direction
G-1-0-0	0°~0°	0°~0°	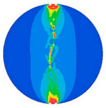	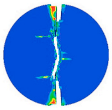	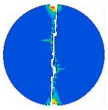
G-2-30-0	-30°~30°	0°~0°	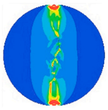	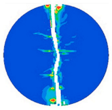	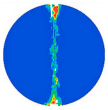
G-3-30-30	-30°~30°	-30°~30°	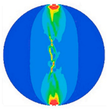	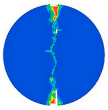	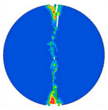
G-4-60-0	-60°~60°	0°~0°	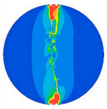	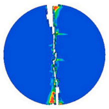	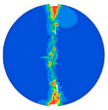
G-5-60-30	-60°~60°	-30°~30°	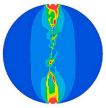	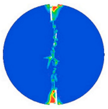	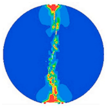
G-6-60-60	-60°~60°	-60°~60°	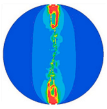	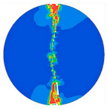	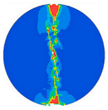
G-7-90-0	-90°~90°	0°~0°	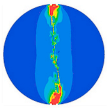	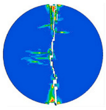	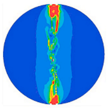
G-8-90-30	-90°~90°	-30°~30°	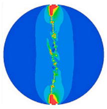	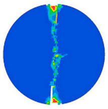	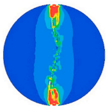
G-9-90-60	-90°~90°	-60°~60°	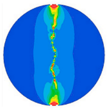	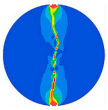	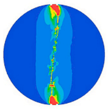
G-10-90-90	-90°~90°	-90°~90°	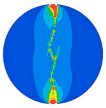	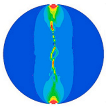	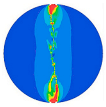

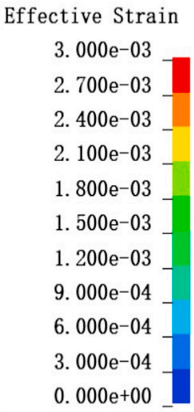

Fig. 17(b) illustrates the variation pattern of compressive strength in different directions for 3D-printed SFRC, with equal increments in the range of angles η and θ. In the X-direction, the compressive strength initially decreases and then increases with the angle range. Notably, when $-60^\circ \le \eta \le 60^\circ$ and $-60^\circ \le \theta \le 60^\circ$, the compressive strength in the X-direction reaches its lowest point at 149.7 MPa. This behaviour can be attributed to a similar phenomenon observed when a single angle increases, as mentioned earlier. Conversely, for the compressive strength in the Y- and Z-directions, the strength values remain similar regardless of changes in the angle range. This is attributed to the consistent orientation of steel fibres in the specimen when compressed from these two directions. Furthermore, it can be observed that the compressive strength in the Y- and Z-directions follows a pattern of initially increasing and then decreasing. By combining this analysis with the earlier examination of the effect of a single angle range change on strength, it is speculated that this behaviour arises from the more pronounced influence of horizontal angle changes when the angle is less than 30°, while vertical angle changes become more significant when the angle exceeds 60°.

5.2.2. *Tension*

The tensile strength of specimens with varying fibre orientations was determined through finite element simulation, as summarized in Table 11. Consistent with Figs. 16 and 18 illustrates the relationship between tensile strength and fibre orientation as the angles η and θ range from [0°, 0°] to [−90°, 90°]. Specifically, Fig. 18(a) depicts the changes in tensile strength for different specimens when subjected to stretching along the X-direction. According to the results of the data, it can be found that the tensile strength in the X-direction exhibits a change law of first increasing and then decreasing, especially as the angle η and θ can

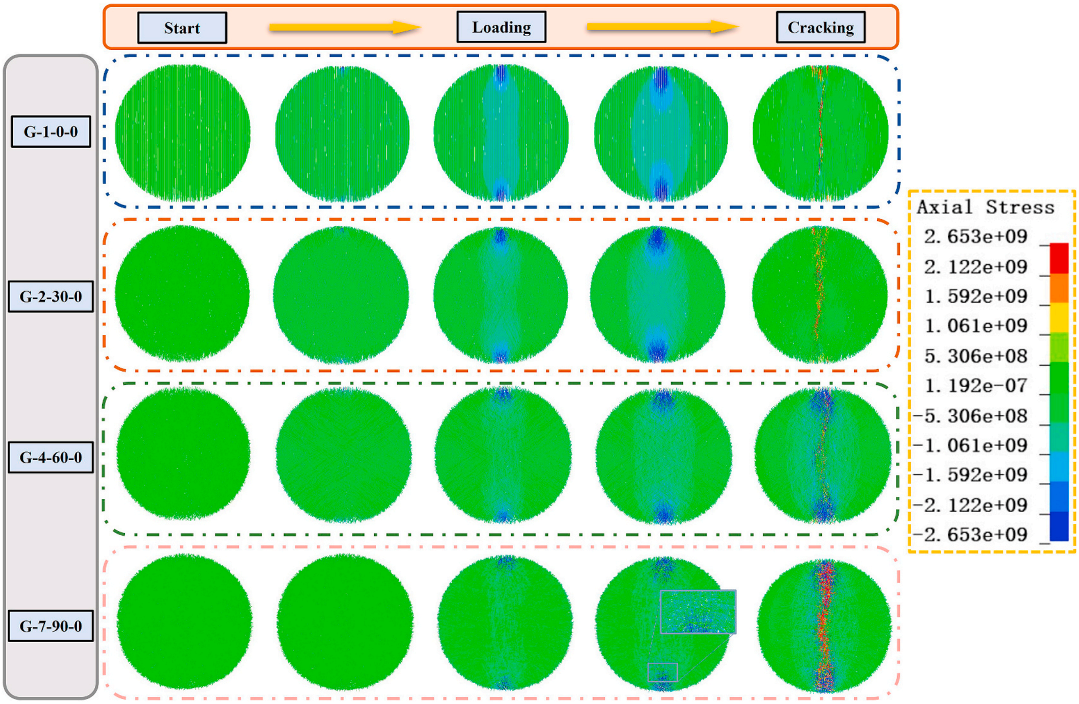

Fig. 15. Axial force nephogram of fibre in the specimen during loading process.

Table 10
Compressive strength of specimens with different fibre orientations.

Group	Distribution interval of angle		The compressive strength in different direction (MPa)		
	η (°)	θ (°)	X-direction	Y-direction	Z-direction
G-1-0-0	0°–0°	0°–0°	171.1	160.4	160.2
G-2-30-0	−30°–30°	0°–0°	159.4	163.5	157.2
G-3-30-30	−30°–30°	−30°–30°	156.6	162.3	162.3
G-4-60-0	−60°–60°	0°–0°	149.5	161.0	154.2
G-5-60-30	−60°–60°	−30°–30°	149.5	163.3	156.2
G-6-60-60	−60°–60°	−60°–60°	149.7	158.0	157.8
G-7-90-0	−90°–90°	0°–0°	152.0	166.9	152.0
G-8-90-30	−90°–90°	−30°–30°	152.3	163.9	153.2
G-9-90-60	−90°–90°	−60°–60°	153.6	159.1	154.7
G-10-90-90	−90°–90°	−90°–90°	155.5	155.3	155.6

reach ±30°, the tensile strength can reach the maximum. When the angles η and θ are in the [−30°, 30°] range at the same time, the tensile strength of SFRC in the X-direction reaches 23.5 MPa. It can be seen from Fig. 4 that the tensile strength of SFRC can reach the maximum value at this time because the pull-out strength at the angle of 30° (the angle between the distribution direction of steel fibre and the pull-out direction) is higher than that at the angles of 0°, 60° and 90°.

Fig. 18 (b) and (c) respectively display the variation in tensile strength of different specimens as tension along the Y- and Z-directions. The two demonstrated similar changes. As tension is applied along the Y-direction, the tensile strength increases with the angle θ regardless of the value range of angle η. Meanwhile, as angle θ is constant, the tensile strength in Y-direction is almost unchanged irrespective of the range of angle η. Similarly, when tension is applied along the Z-direction, the tensile strength increases with the angle η regardless of the value range of angle θ. As the angle η is constant, the tensile strength in the Z-direction is almost unchanged irrespective of the value range of angle θ. The main reason for this rule is that as the vertical angle (the tensile direction is the vertical direction) is unchanged, the change in the horizontal angle (the plane perpendicular to the tensile direction is the horizontal plane) does not affect the pull-out resistance of steel fibres.

To more intuitively explore the change rule of tensile strength under different tensile directions owing to the change in fibre orientation range, Fig. 19 also shows the strength of “one angle range remains unchanged while the other angle range increases” and “both angle ranges increase together".

Fig. 19 (a) depicts the variation in tensile strength in different directions for an angle θ of 0°, with an increased range of angle η. Notably, the tensile strength in the X-, Y-, and Z-directions demonstrates distinct patterns of change. Specifically, the tensile strength in the X-direction initially increases and then decreases as the angle η increases. Conversely, the tensile strength in the Y-direction remains constant regardless of changes in angle η. In contrast, the tensile strength in the Z-direction increases with angle η. Furthermore, when the angle η is 0°, the tensile strength in the Y-direction is equivalent to that in the Z-direction. Similarly, within the range of $-90^\circ \leq \eta \leq 90^\circ$, the tensile strength in the X-direction matches that in the Z-direction. Notably, when $-30^\circ \leq \eta \leq 30^\circ$, the tensile strength in the X-direction is 177.33 % higher than that in the Y-direction and 106.06 % higher than that in the Z-direction.

Fig. 19 (b) presents the tensile strength in different directions with the same increase in angles η and θ. Herein, the tensile strength in Y-direction and Z-direction exhibits the same change rule, and both increase with the angle range. However, the variation rule of tensile strength in X-direction is different from that in the other two, which indicates the rule of first increasing and then decreasing.

To sum up, the orientation change of steel fibres has a significant impact on the anisotropy of the tensile strength of 3D-printed SFRC.

6. Conclusion

In this study, an analysis was conducted on the distribution of steel fibres in 3D-printed SFRC and the relationship between steel fibre orientation, nozzle size, and printing parameters. Additionally, meso-scale finite element models were developed to simulate 3D-printed SFRC with different steel fibre orientations, and the simulation results were compared with experimental data. Through a parametric analysis using these models, the effects of steel fibre orientation on the performance of 3D-printed SFRC were investigated. The key findings are as follows.

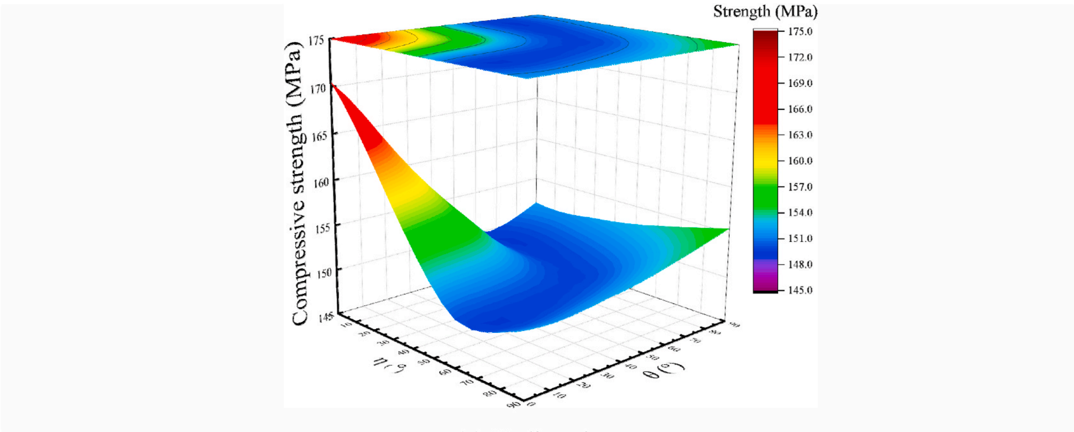

(a) X-direction

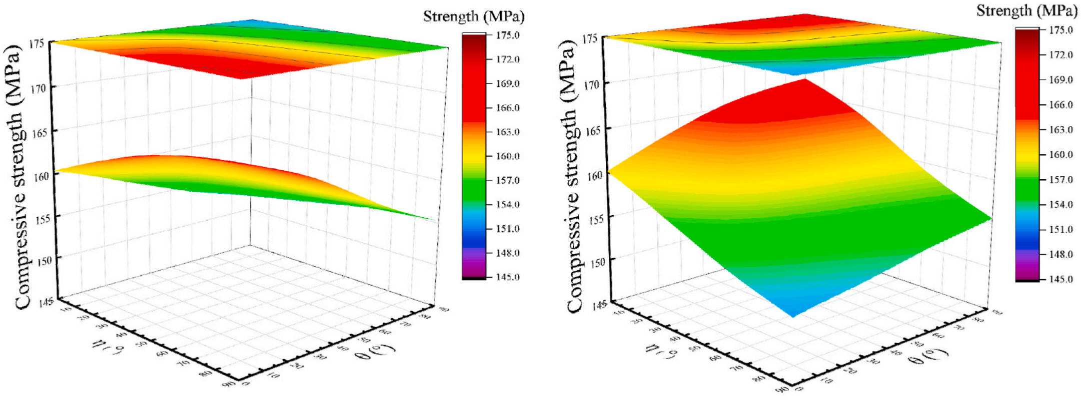

(b) Y-direction (c) Z-direction

Fig. 16. The variation in compressive strength in different directions with changes in fibre orientation.

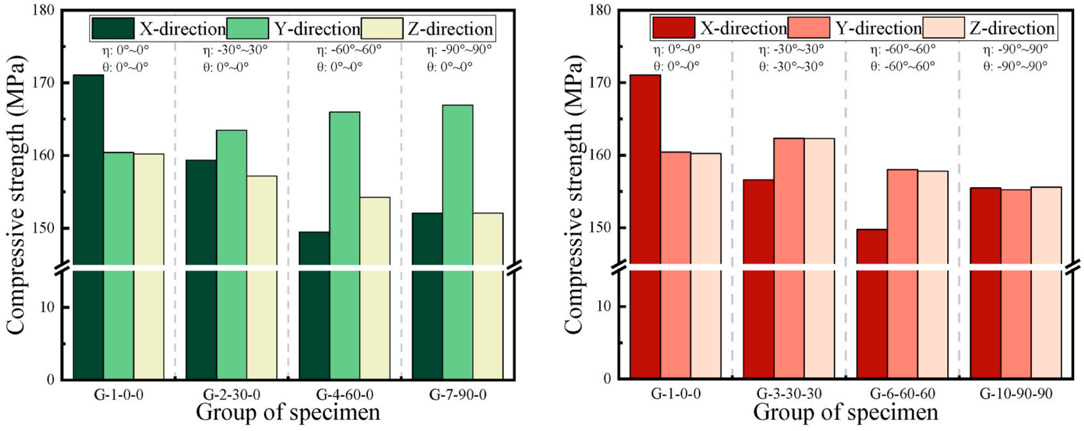

(a) Single angle range increase (b) Two angle range increase

Fig. 17. The influence of fibre orientation range change on compressive strength.

(1) For 3D-printed concrete, observations from different studies reveal that the steel fibre content within the range of angles η (0°–30°) is greater than 90 % when using a circular nozzle for vertical extrusion. Regarding the angle θ, as the nozzle diameter increases, the proportion of steel fibre content within the range of angles θ (0°–30°) gradually decreases, resulting in less pronounced orientation effects;

(2) For compression, steel fibre orientation has a remarkable effect on the compressive damage mode. By adjusting the orientation of steel fibre, the compressive damage mode can be adjusted. For example, when the value range of angles η and θ is not greater than 30°, the damage mode exhibits annular damage, while the value range of angle η and angle θ is greater than 60°, the damage mode shows through crack;

Table 11
Tensile strength of specimens with different fibre orientations.

Group	Distribution interval of angle		The tensile strength in different direction (MPa)		
	η (°)	θ (°)	X-direction	Y-direction	Z-direction
G-1-0-0	0°–0°	0°–0°	20.142	8.474	8.634
G-2-30-0	−30°–30°	0°–0°	23.429	8.448	11.370
G-3-30-30	−30°–30°	−30°–30°	23.521	11.304	11.334
G-4-60-0	−60°–60°	0°–0°	22.098	8.430	13.857
G-5-60-30	−60°–60°	−30°–30°	21.542	11.115	14.171
G-6-60-60	−60°–60°	−60°–60°	19.476	14.325	14.241
G-7-90-0	−90°–90°	0°–0°	16.792	8.465	16.835
G-8-90-30	−90°–90°	−30°–30°	18.129	11.440	16.718
G-9-90-60	−90°–90°	−60°–60°	17.071	14.549	16.582
G-10-90-90	−90°–90°	−90°–90°	16.544	16.156	16.582

(3) For tension, as the distributed direction of steel fibres is perpendicular to the tensile direction or as the angle between the distributed direction of steel fibres and the tensile direction exceeds 60°, the restraining effect of steel fibres on concrete cracking is relatively low, resulting in less ductile damage in 3D-printed SFRC. However, as many steel fibres are aligned at angles smaller than 60°, they may cause ductile damage in 3D-printed SFRC. Thus, steel fibre orientation has a decisive influence on the damage pattern of 3D-printed SFRC;

(4) Increasing the range of horizontal azimuth angles enhances the compressive strength of SFRC, while increasing the range of vertical azimuth angles reduces its compressive strength. For instance, the compressive strength in the Y-direction achieves its maximum value when $-90° \leq \eta \leq 90°$, exhibiting a 4.06 % increase as compared to $\eta = 0°$. On the other hand, the compressive strength in the Z-direction reaches its minimum value when $-90° \leq \eta \leq 90°$, exhibiting a 5.10 % decrease as compared to $\eta = 0°$;

(5) When the angle θ is 0° and the range of angle η increases, the tensile strength in the Y- and Z-directions is equal when angle η is 0°, while the tensile strength in the X- and Z-directions is equal when $-90° \leq \eta \leq 90°$;

This study aims to provide a theoretical basis for understanding the influence of steel fibre orientation distribution on the performance of 3D-printed SFRC. However, despite the exciting results obtained in this research, there are still some limitations. For instance, the distribution of steel fibres in this study is in an ideal state and does not consider complex distribution scenarios. Future research can integrate CT scanning and machine learning techniques to predict and calculate the specific distribution range of steel fibres in 3D-printed SFRC, and establish a formula that relates fibre orientation to performance.

CRediT authorship contribution statement

Yekai Yang: Writing – review & editing, Writing – original draft, Methodology, Investigation, Conceptualization. **Chengqing Wu:** Writing – review & editing, Visualization, Supervision, Methodology, Conceptualization.

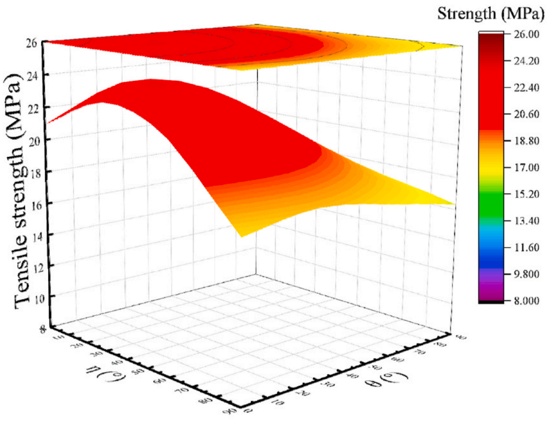

(a) X-direction

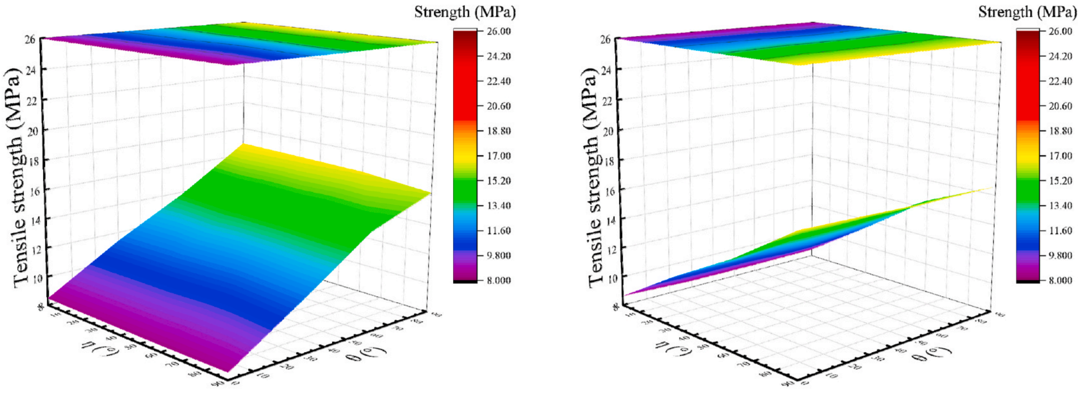

(b) Y-direction

(c) Z-direction

Fig. 18. Variation in tensile strength in different directions with changes in fibre orientation.

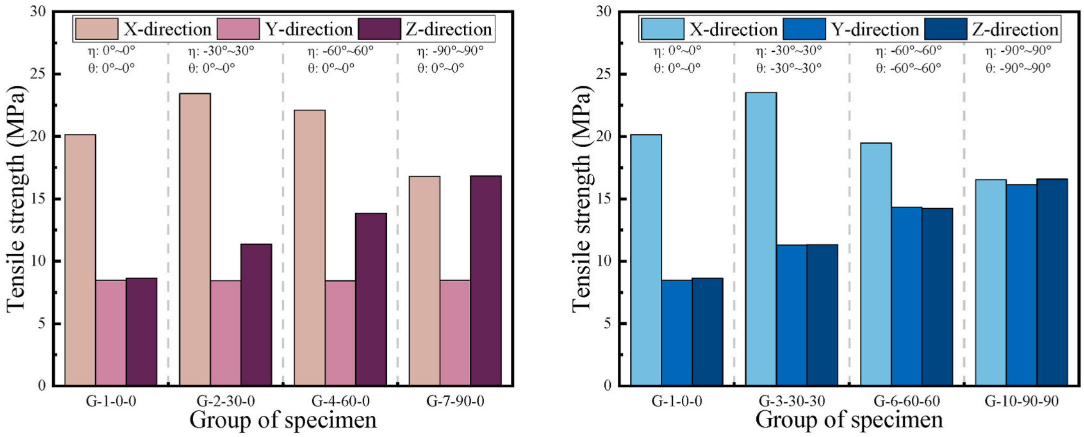

(a) Single angle range increase

(b) Two angle range increase

Fig. 19. The influence of fibre orientation range change on tensile strength.

Declaration of competing interest

We confirm that the manuscript has been read and approved by all named authors and that there are no other persons who satisfied the criteria for authorship but are not listed. We further confirm that the order of authors listed in the manuscript has been approved by all of us.

We confirm that we have given due consideration to the protection of intellectual property associated with this work and that there are no impediments to publication, including the timing of publication, with respect to intellectual property. In doing so we confirm that we have followed the regulations of our institutions concerning intellectual property.

We understand that the Corresponding Author is the sole contact for the Editorial process (including Editorial Manager and direct communications with the office). He is responsible for communicating with the other authors about progress, submissions of revisions and final approval of proofs. We confirm that we have provided a current, correct email address which is accessible by the Corresponding Author and which has been configured to accept email from Chengqing.wu@uts.edu.au.

Data availability

Data will be made available on request.

Acknowledgement

The research presented herein is supported by the National Natural Science Foundation of China (Grant No. 52108251, Grant No.51978186), the Natural Science Foundation of Hebei Province (Grant No. E2021203141), the Science and Technology Project of Hebei Education Department (Grant No. QN2023190).

References

[1] S.A. Khan, M. Koç, S.G. Al-Ghamdi, Sustainability assessment, potentials and challenges of 3D printed concrete structures: a systematic review for built environmental applications, J. Clean. Prod. 303 (2021) 127027.
[2] G. De Schutter, K. Lesage, V. Mechtcherine, V.N. Nerella, G. Habert, I. Agusti-Juan, Vision of 3D printing with concrete—technical, economic and environmental potentials, Cement Concr. Res. 112 (2018) 25–36.
[3] M.T. Souza, I.M. Ferreira, E.G. de Moraes, L. Senff, A.P.N. de Oliveira, 3D printed concrete for large-scale buildings: an overview of rheology, printing parameters, chemical admixtures, reinforcements, and economic and environmental prospects, J. Build. Eng. 32 (2020) 101833.
[4] A.S. Alchaar, A.K. Al-Tamimi, Mechanical properties of 3D printed concrete in hot temperatures, Construct. Build. Mater. 266 (2021) 120991.
[5] X. Huang, W. Yang, F. Song, J. Zou, Study on the mechanical properties of 3D printing concrete layers and the mechanism of influence of printing parameters, Construct. Build. Mater. 335 (2022) 127496.
[6] R.J.M. Wolfs, F.P. Bos, T.A.M. Salet, Hardened properties of 3D printed concrete: the influence of process parameters on interlayer adhesion, Cement Concr. Res. 119 (2019) 132–140.
[7] J. Xiao, H. Liu, T. Ding, Finite element analysis on the anisotropic behavior of 3D printed concrete under compression and flexure, Addit. Manuf. 39 (2021) 101712.
[8] J. Kruger, A. du Plessis, G. van Zijl, An investigation into the porosity of extrusion-based 3D printed concrete, Addit. Manuf. 37 (2021) 101740.
[9] M.K. Mohan, A.V. Rahul, G. De Schutter, K. Van Tittelboom, Extrusion-based concrete 3D printing from a material perspective: a state-of-the-art review, Cement Concr. Compos. 115 (2021) 103855.
[10] J. Van Der Putten, D. Snoeck, R. De Coensel, G. De Schutter, K. Van Tittelboom, Early age shrinkage phenomena of 3D printed cementitious materials with superabsorbent polymers, J. Build. Eng. 35 (2021) 102059.
[11] M.V. Tran, Y.T. Cu, C.V. Le, Rheology and shrinkage of concrete using polypropylene fiber for 3D concrete printing, J. Build. Eng. 44 (2021) 103400.
[12] T. Ding, J. Xiao, S. Zou, J. Yu, Flexural properties of 3D printed fibre-reinforced concrete with recycled sand, Construct. Build. Mater. 288 (2021) 123077.
[13] R. Yang, Q. Zeng, Y. Peng, H. Wang, Z. Wang, Anomalous matrix and interlayer pore structure of 3D-printed fiber-reinforced cementitious composites, Cement Concr. Res. 157 (2022) 106829.
[14] Butterworth-Heinemann, B. Panda, S.C. Paul, M.J. Tan, Anisotropic mechanical performance of 3D printed fiber reinforced sustainable construction material, Mater. Lett. 209 (2017) 146–149.
[15] Y. Yang, C. Wu, Z. Liu, H. Wang, Q. Ren, Mechanical anisotropy of ultra-high performance fibre-reinforced concrete for 3D printing, Cement Concr. Compos. 125 (2022) 104310.
[16] Y. Yang, C. Wu, Z. Liu, H. Zhang, 3D-printing ultra-high performance fiber-reinforced concrete under triaxial confining loads, Addit. Manuf. 50 (2022) 102568.
[17] Y. Yang, C. Wu, Z. Liu, J. Li, T. Yang, X. Jiang, Characteristics of 3D-printing ultra-high performance fibre-reinforced concrete under impact loading, Int. J. Impact Eng. 164 (2022) 104205.
[18] L. Dong, Y. Yang, Z. Liu, Q. Ren, J. Li, Y. Zhang, C. Wu, Microstructure and mechanical behaviour of 3D printed ultra-high performance concrete after elevated temperatures, Addit. Manuf. 58 (2022) 103032.
[19] L. Pham, P. Tran, J. Sanjayan, Steel fibres reinforced 3D printed concrete: influence of fibre sizes on mechanical performance, Construct. Build. Mater. 250 (2020) 118785.
[20] A. Singh, Q. Liu, J. Xiao, Q. Lyu, Mechanical and macrostructural properties of 3D printed concrete dosed with steel fibers under different loading direction, Construct. Build. Mater. 323 (2022) 126616.
[21] I. Giwa, D. Game, H. Ahmed, H. Noorvand, G. Arce, M. Hassan, A. Kazemian, Performance and macrostructural characterization of 3D printed steel fiber reinforced cementitious materials, Construct. Build. Mater. 369 (2023) 130593.
[22] Y. Chen, Y. Zhang, B. Pang, D. Wang, Z. Liu, G. Liu, Steel fiber orientational distribution and effects on 3D printed concrete with coarse aggregate, Mater. Struct. 55 (3) (2022) 100.
[23] F.P. Bos, E. Bosco, T.A.M. Salet, Ductility of 3D printed concrete reinforced with short straight steel fibers, Virtual Phys. Prototyp. 14 (2) (2019) 160–174.
[24] M.J.H. Wijffels, R.J.M. Wolfs, A.S.J. Suiker, T.A.M. Salet, Magnetic orientation of steel fibres in self-compacting concrete beams: effect on failure behaviour, Cement Concr. Compos. 80 (2017) 342–355.
[25] R. Mu, H. Li, L. Qing, J. Lin, Q. Zhao, Aligning steel fibers in cement mortar using electro-magnetic field, Construct. Build. Mater. 131 (2017) 309–316.
[26] H. Huang, X. Gao, A. Zhang, Numerical simulation and visualization of motion and orientation of steel fibers in UHPC under controlling flow condition, Construct. Build. Mater. 199 (2019) 624–636.

[27] H. Huang, X. Gao, K.H. Khayat, Contribution of fiber orientation to enhancing dynamic properties of UHPC under impact loading, Cement Concr. Compos. 121 (2021) 104108.

[28] A.R. Arunothayan, B. Nematollahi, R. Ranade, J.G. Sanjayan, K.H. Khayat, Fiber orientation effects on ultra-high performance concrete formed by 3D printing, Cement Concr. Res. 143 (2021) 106384.

[29] J. Zhou, J. Lai, L. Du, K. Wu, S. Dong, Effect of directionally distributed steel fiber on static and dynamic properties of 3D printed cementitious composite, Construct. Build. Mater. 318 (2022) 125948.

[30] W. Yu, L. Jin, X. Du, Influence of pre-static loads on dynamic compression and corresponding size effect of concrete: mesoscale analysis, Construct. Build. Mater. 300 (2021) 124302.

[31] X. Du, L. Jin, G. Ma, Meso-element equivalent method for the simulation of macro mechanical properties of concrete, Int. J. Damage Mech. 22 (5) (2013) 617–642.

[32] M. Congro, D. Roehl, E.C. Sanchez, Computational mesoscale modeling for the mechanical behavior of fiber reinforced concrete. In Fibre Reinforced Concrete: Improvements and Innovations II, X RILEM-fib Int. Sympos. Fibre Reinforc. Concrete (BEFIB) 10 (2022) 357–364, 2021.

[33] L.A. Bitencourt Jr, O.L. Manzoli, T.N. Bittencourt, F.J. Vecchio, Numerical modeling of steel fiber reinforced concrete with a discrete and explicit representation of steel fibers, Int. J. Solid Struct. 159 (2019) 171–190.

[34] M. Congro, D. Roehl, C. Mejia, Mesoscale computational modeling of the mechanical behavior of cement composite materials, Compos. Struct. 257 (2021) 113137. Congro, M., Sanchez, E. C. M., Roehl, D., & Marangon, E. (2019). Fracture modeling of fiber reinforced concrete in a multiscale approach. Composites Part B: Engineering, 174, 106958.

[35] Y. Peng, C. Wu, J. Li, J. Liu, X. Liang, Mesoscale analysis on ultra-high performance steel fibre reinforced concrete slabs under contact explosions, Compos. Struct. 228 (2019) 111322.

[36] M. Xu, K. Wille, Calibration of K&C concrete model for UHPC in LS-DYNA, Adv. Mater. Res. 1081 (2015) 254–259.

[37] L.E. Schwer, L.J. Malvar, Simplified Concrete Modeling with* MAT_CONCRETE_DAMAGE_REL3, JRI LS-Dyna User Week, 2005, pp. 49–60.

[38] J.M. Magallanes, Y. Wu, L.J. Malvar, J.E. Crawford, Recent improvements to release III of the K&C concrete model, in: 11th International LS-DYNA Users Conference, vol. 1, Livermore Software Technology Corporation, Livermore, CA, 2010, June, pp. 37–48. No. 3.

[39] M. Xu, K. Wille, Calibration of K&C concrete model for UHPC in LS-DYNA, in: Advanced Materials Research vol. 1081, Trans Tech Publications Ltd, 2015, pp. 254–259. ,33.

[40] S. Xu, P. Wu, C. Wu, Calibration of KCC concrete model for UHPC against low-velocity impact, Int. J. Impact Eng. 144 (2020) 103648.

[41] X. Liang, C. Wu, Meso-scale modelling of steel fibre reinforced concrete with high strength, Construct. Build. Mater. 165 (2018) 187–198.

[42] M. Xu, K. Wille, Calibration of K&C concrete model for UHPC in LS-DYNA, Adv. Mater. Res. 1081 (2015) 254–259.

[43] M. Unosson, L. Nilsson, Projectile penetration and perforation of high performance concrete: experimental results and macroscopic modelling, Int. J. Impact Eng. 32 (7) (2006) 1068–1085.

[44] Y. Liu, Z. Zhang, C. Shi, D. Zhu, N. Li, Y. Deng, Development of ultra-high performance geopolymer concrete (UHPGC): influence of steel fiber on mechanical properties, Cement Concr. Compos. 112 (2020) 103670.

[45] W. Abbass, M.I. Khan, S. Mourad, Evaluation of mechanical properties of steel fiber reinforced concrete with different strengths of concrete, Construct. Build. Mater. 168 (2018) 556–569.

[46] Y. Yang, C. Wu, Z. Liu, Rate dependent behaviour of 3D printed ultra-high performance fibre-reinforced concrete under dynamic splitting tensile, Compos. Struct. 309 (2023) 116727.

[47] Y. Su, J. Li, C. Wu, P. Wu, M. Tao, X. Li, Mesoscale study of steel fibre-reinforced ultra-high performance concrete under static and dynamic loads, Mater. Des. 116 (2017) 340–351.

[48] H. Zhang, Y.J. Huang, Z.J. Yang, F.Q. Guo, L.H. Shen, 3D meso-scale investigation of ultra high performance fibre reinforced concrete (UHPFRC) using cohesive crack model and Weibull random field, Construct. Build. Mater. 327 (2022) 127013.

[49] Y. Lee, S.T. Kang, J.K. Kim, Pullout behavior of inclined steel fiber in an ultra-high strength cementitious matrix, Construct. Build. Mater. 24 (10) (2010) 2030–2041.

[50] S. Muthukrishnan, S. Ramakrishnan, J. Sanjayan, Technologies for improving buildability in 3D concrete printing, Cement Concr. Compos. 122 (2021) 104144.

[51] V.N. Nerella, S. Hempel, V. Mechtcherine, Effects of layer-interface properties on mechanical performance of concrete elements produced by extrusion-based 3D-printing, Construct. Build. Mater. 205 (2019) 586–601.

[52] H. Gou, H. Zhu, H. Zhou, Z. Yang, Reinforcement mechanism of orientally distributed steel fibers on ultra-high-performance concrete, Construct. Build. Mater. 281 (2021) 122646.